nature methods

ARTICLES

https://doi.org/10.1038/s41592-022-01468-5

A hybrid open-top light-sheet microscope for versatile multi-scale imaging of cleared tissues

Adam K. Glaser[1,2]✉, Kevin W. Bishop[1,3], Lindsey A. Barner[1], Etsuo A. Susaki[4,5], Shimpei I. Kubota[6,7], Gan Gao[1], Robert B. Serafin[1], Pooja Balaram[8], Emily Turschak[8], Philip R. Nicovich[9], Hoyin Lai[10], Luciano A. G. Lucas[10], Yating Yi[11], Eva K. Nichols[12], Hongyi Huang[1], Nicholas P. Reder[1,13], Jasmine J. Wilson[14], Ramya Sivakumar[14], Elya Shamskhou[14], Caleb R. Stoltzfus[14], Xing Wei[15], Andrew K. Hempton[16], Marko Pende[17], Prayag Murawala[17,18], Hans-Ulrich Dodt[19,20], Takato Imaizumi[16], Jay Shendure[12,21,22,23], Brian J. Beliveau[12,23], Michael Y. Gerner[14], Li Xin[15], Hu Zhao[11], Lawrence D. True[13], R. Clay Reid[8], Jayaram Chandrashekar[2,24], Hiroki R. Ueda[5,25], Karel Svoboda[2] and Jonathan T. C. Liu[1,3,13]✉

Light-sheet microscopy has emerged as the preferred means for high-throughput volumetric imaging of cleared tissues. However, there is a need for a flexible system that can address imaging applications with varied requirements in terms of resolution, sample size, tissue-clearing protocol, and transparent sample-holder material. Here, we present a 'hybrid' system that combines a unique non-orthogonal dual-objective and conventional (orthogonal) open-top light-sheet (OTLS) architecture for versatile multi-scale volumetric imaging. We demonstrate efficient screening and targeted sub-micrometer imaging of sparse axons within an intact, cleared mouse brain. The same system enables high-throughput automated imaging of multiple specimens, as spotlighted by a quantitative multi-scale analysis of brain metastases. Compared with existing academic and commercial light-sheet microscopy systems, our hybrid OTLS system provides a unique combination of versatility and performance necessary to satisfy the diverse requirements of a growing number of cleared-tissue imaging applications.

Recent advances in tissue-clearing protocols greatly reduce optical scattering, aberrations, and background fluorescence, enabling deep-tissue imaging with high resolution and contrast. These approaches have yielded new insights in many fields, including neuroscience, developmental biology, and anatomic pathology[1–10]. Light-sheet microscopy has emerged as a preferred means of high-resolution volumetric imaging of cleared tissues owing to its unrivaled speed and low photobleaching[11,12]. Many variants of light-sheet microscopes have been developed in recent years by academic researchers and commercial entities to tackle a diverse range of imaging applications (Supplementary Tables 1 and 2)[13–18]. Whereas individual light-sheet systems are well-suited for a subset of cleared-tissue applications, trade-offs are inevitable. In particular, no current light-sheet microscope can satisfy all of the following requirements: (1) user-friendly mounting of multiple specimens with standard holders, (2) compatibility with all current clearing protocols, (3) no fundamental limits on lateral specimen size, (4) a large imaging depth to accommodate intact mouse organs and thick tissue slabs, and (5) broad 'multi-scale' imaging capabilities for time- and data-efficient workflows. The ability to rapidly screen large (centimeter-scale) tissue volumes at several-micrometer resolution (that is, mesoscopic imaging), along with the ability to quantify fine structures within localized regions of interest (millimeter-scale regions) at sub-micrometer resolution, would be of great value.

The majority of cleared-tissue microscopes use an illumination objective that is oriented in the horizontal plane of the specimen, along with a collection objective that is orthogonal to the illumination objective, that is, an orthogonal dual-objective (ODO) configuration[13,15,18] (Fig. 1a). This imaging geometry places physical constraints on the lateral size of the specimen such that it is not possible to image large, centimeter-scale tissue slabs

[1]Department of Mechanical Engineering, University of Washington, Seattle, WA, USA. [2]Allen Institute for Neural Dynamics, Seattle, WA, USA. [3]Department of Bioengineering, University of Washington, Seattle, WA, USA. [4]Department of Biochemistry and Systems Biomedicine, Graduate School of Medicine, Juntendo University, Tokyo, Japan. [5]Laboratory for Synthetic Biology, RIKEN Center for Biosystems Dynamics Research, Osaka, Japan. [6]Department of Molecular Pathology, Graduate School of Medicine, The University of Tokyo, Tokyo, Japan. [7]Division of Molecular Psychoimmunology, Institute for Genetic Medicine, Graduate School of Medicine, Hokkaido University, Sapporo, Japan. [8]Allen Institute for Brain Science, Seattle, WA, USA. [9]Cajal Neuroscience, Seattle, WA, USA. [10]Leica Microsystems, Inc, Buffalo Grove, IL, USA. [11]Department of Restorative Sciences, Texas A&M University, Dallas, TX, USA. [12]Department of Genome Sciences, University of Washington, Seattle, WA, USA. [13]Department of Laboratory Medicine & Pathology, University of Washington, Seattle, WA, USA. [14]Department of Immunology, University of Washington, Seattle, WA, USA. [15]Department of Urology, University of Washington, Seattle, WA, USA. [16]Department of Biology, University of Washington, Seattle, WA, USA. [17]MDI Biological Laboratory, Bar Harbor, ME, USA. [18]Clinic for Kidney and Hypertension Diseases, Hannover Medical School, Hannover, Germany. [19]Department for Bioelectronics, Vienna University of Technology, Vienna, Austria. [20]Section for Bioelectronics, Center for Brain Research, Medical University of Vienna, Vienna, Austria. [21]Howard Hughes Medical Institute, Seattle, WA, USA. [22]Allen Discovery Center for Cell Lineage Tracing, Seattle, WA, USA. [23]Brotman Baty Institute for Precision Medicine, Seattle, WA, USA. [24]Janelia Research Campus, Howard Hughes Medical Institute, Ashburn, VA, USA. [25]Department of Systems Pharmacology, Graduate School of Medicine, The University of Tokyo, Tokyo, Japan. ✉e-mail: akglaser@uw.edu; jonliu@uw.edu

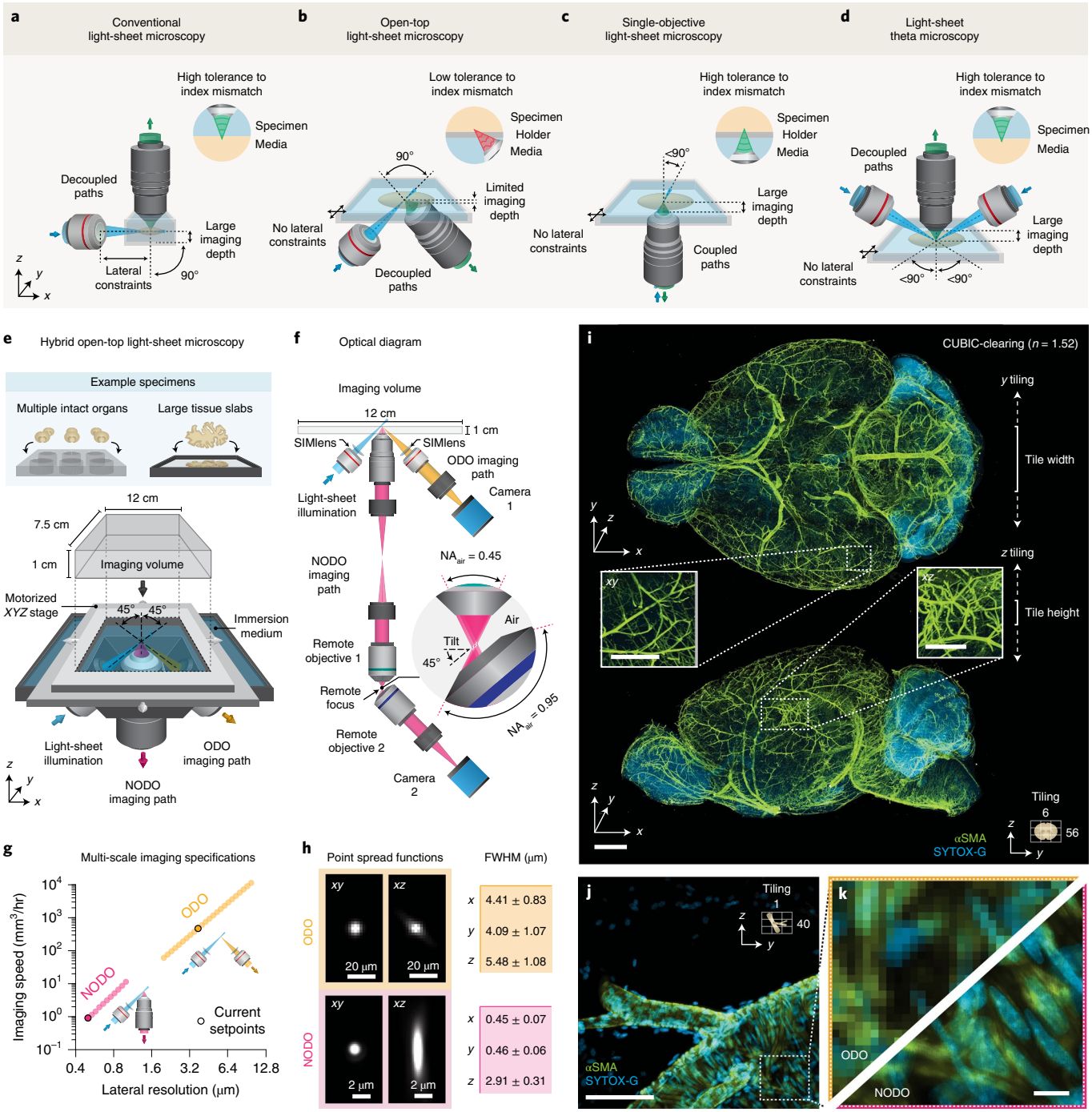

Fig. 1 | Hybrid OTLS microscopy. a–d, Optical layouts of conventional, open-top, single-objective, and theta light-sheet microscopy systems. Aspects of each microscope architecture, including number and orientation of objectives, lateral constraints on specimen size, maximum imaging depth, and tolerance to index mismatch are highlighted. **e–f**, Our hybrid microscope architecture consists of three objectives positioned below the specimen. One objective is used for light-sheet illumination, and the other two objectives are used for orthogonal dual-objective (ODO) and non-orthogonal dual-objective (NODO) imaging. By using a motorized stage, tiled imaging is possible with both paths over a large 12 × 7.5 × 1 cm (*XYZ*) imaging volume, accommodating multiple intact cleared organs and large tissue slabs mounted in an array of specimen holders. **g**, In combination, the ODO and NODO paths enable imaging over a tunable lateral resolution range of 0.5–10.7 μm at imaging speeds of ~5 mm^3 to 10 cm^3 per hour. The current set points of the system are highlighted. **h**, At these set points, the mean ± standard deviation full-width half-maximum (FWHM) resolutions (*xyz*) for the ODO path are 4.09 ± 1.07, 4.41 ± 0.83, and 5.48 ± 1.08 μm (n = 109 beads), and for the NODO path are 0.45 ± 0.07, 0.46 ± 0.06, and 2.91 ± 0.31 μm (n = 437 beads). **i**, Representative ODO imaging results of an entire intact CUBIC-cleared mouse brain with arterial (αSMA) and nuclear (SYTOX-G) staining. The ODO imaging path is able to clearly resolve vasculature in both the *xy* and *xz* planes (insets). The size and direction of tiling is annotated. **j**,**k**, Targeted NODO imaging of a sub-region centered on a branching arteriole resolves individual smooth muscle cells and sub-nuclear features that are not resolved by ODO imaging. Scale-bar lengths are as follows: **i**, 1 mm (insets, 500 μm); **j**, 100 μm; and **k**, 10 μm. All images are displayed without deconvolution. The imaging data in **i**–**k** were acquired from a single mouse brain in a single experiment.

or multiple specimens mounted in standard holders (for example, well plates). Therefore, we and others have previously developed ODO systems with an inverted geometry (Supplementary Fig. 1), which overcomes these constraints by tilting both objectives and placing them above or below the specimen[19–26] (Fig. 1b). In particular, open-top light-sheet (OTLS) microscopy systems provide an ease-of-use similar to a flat-bed document scanner by placing all optical components below the sample holder[21–26]. This enables the use of a wide range of modular sample holders, as well as potential accessory technologies, such as microfluidics, electrophysiology, and microdissection and aspiration devices. With OTLS systems, the angled orientation of the objectives reduces the usable imaging depth of the systems to well below each objective's native working distance. In addition, in OTLS microscopy, angling the optical paths with respect to a horizontal sample holder can introduce significant off-axis aberrations (especially for higher-numerical-aperture beams) unless the refractive index of the specimen and the sample holder are exquisitely well-matched. This can reduce the ease of use and versatility of high-numerical-aperture (high-NA) OTLS systems.

To overcome these issues, we considered the use of a single-objective architecture that has gained popularity in recent years. In these systems, the illumination and collection beams share a single objective and are non-orthogonal to one another, requiring a method such as remote refocusing to rectify the imaging plane[27–38] (Fig. 1c). Orienting the objective in the vertical direction with respect to a horizontal specimen holder makes use of the objective's full working distance and dramatically increases the system's tolerance to refractive-index mismatch (Supplementary Fig. 2). However, single-objective microscopy is incompatible with multi-scale imaging because, to the best of our knowledge, no currently available objective provides both sub-micrometer resolution and a large field of view of up to 1 cm. In addition, the use of a single objective both constrains and couples the illumination and collection beams such that there is less flexibility to tailor the axial and lateral resolutions (Supplementary Fig. 3)[39]. More recently, the light-sheet theta microscope (LSTM) was developed (Fig. 1d), which also features a non-orthogonal configuration. In LSTM, a high-NA collection objective is oriented in the vertical direction (similar to single-objective microscopy), but a separate pair of angled objectives are used for lower-NA light-sheet illumination[14]. While this design decouples the illumination and collection beams, the imaging approach sacrifices light-collection efficiency (see Supplementary Note 1) and has not been demonstrated for broad multi-scale imaging.

To address the varied requirements of cleared-tissue light-sheet microscopists, we designed a 'hybrid' OTLS microscope. Our new hybrid system leverages the strengths and overcomes the limitations of previous systems (Supplementary Note 2), addressing the five requirements listed earlier: (1) simple open-top mounting of multiple specimens in standard holders, such as well plates, (2) the ability to pair any tissue-clearing reagent with nearly any sample-holder material with negligible degradation in imaging performance (that is, high tolerance to refractive-index mismatch, Supplementary Figs. 4 and 5), (3) no lateral constraints on the specimen size (limited only by the travel range of the microscope stage), (4) a 1-cm maximum imaging depth for comprehensive interrogation of intact mouse organs and thick tissue slabs, and (5) multi-scale imaging over a range roughly corresponding to what is achieved with ×2 to ×40 objectives. These unique capabilities open the door for new light-sheet microscopy experiments. Using our hybrid OTLS system, we demonstrate efficient volumetric imaging workflows in which cleared tissues are screened rapidly at low resolution to identify sparse biological structures (for example, axons and metastatic cancer cells) for subsequent quantitative interrogation with sub-micrometer resolution.

Results

System design. The layout of our new system is shown in Fig. 1e. The system architecture features three main objectives that are selected to avoid geometric interference. All three objectives are positioned below the specimen, which provides an unobstructed open top that enables three-dimensional (3D) imaging over a large 12 × 7.5 × 1 cm (*xyz*) imaging volume. The imaging volume is limited in *z* by the objectives and in *xy* by the mechanical limits of the motorized stage. All three objectives are sealed into a monolithic imaging chamber through direct immersion or the use of a solid-immersion meniscus lens (SIMlens), which provides multi-immersion capabilities spanning the refractive index range of all current clearing protocols (Supplementary Fig. 6)[25,26].

The optical layout of the system is shown in Fig. 1f. To achieve an optimal combination of sub-micrometer resolution, large imaging depth, and compatibility with standard sample holders, we developed a new non-orthogonal dual-objective (NODO) light-sheet configuration that features a non-orthogonal arrangement of illumination and collection objectives along with remote refocusing to rectify the imaging plane[39]. By using the full numerical aperture (NA) of a vertically oriented objective for fluorescence collection and a separate objective for non-orthogonal illumination, our new NODO architecture provides superior resolution to that of a single-objective light-sheet system (if based on the same primary objective) and relaxes the NA requirements for the remote focus module that is necessary for these non-orthogonal light-sheet systems (Supplementary Fig. 3). This allows for the use of a wider range of moderate-NA primary (collection) objectives for cleared-tissue imaging, as well as simple air objectives at the remote focus module rather than bespoke objective assemblies (Supplementary Fig. 7). In addition, by using remote refocusing to image the light sheet onto a camera, this design provides roughly ten times more light-efficient imaging than does LSTM, even when considering the additional optical elements required for remote refocusing (Supplementary Note 1 and Supplementary Fig. 8). We carefully selected our NODO collection objective and its optical and mechanical specifications to enable the placement of a separate low-NA collection objective oriented orthogonally to the illumination objective (Supplementary Fig. 9). This forms an additional ODO imaging path for rapid imaging with mesoscopic (that is, several-micrometer) resolution. Unlike the NODO configuration, the ODO collection path directly images the orthogonal light sheet onto a camera. By varying the light sheet width, the same illumination path is used for both NODO and ODO imaging modes. Supplementary Figs. 10–17 and Supplementary Video 1 contain optical models, a photograph of the hybrid OTLS microscope, and additional point spread functions for both imaging paths.

The overall magnification of each imaging path is tunable, limited at the extremes by either the NA or field of view (FOV) of the collection objectives (see Supplementary Note 3 for further discussion of these two imaging modes), corresponding to a combined lateral-resolution range of ~0.4–10 µm, and volumetric imaging speeds of ~1 mm^3 to 4 cm^3 per hour (Fig. 1g). In the current microscope configuration, the NODO path provides an *xyz* resolution of 0.45 ± 0.07, 0.46 ± 0.05, and 2.91 ± 0.31 µm ($n = 437$ beads), and the ODO path provides an *xyz* resolution of 4.41 ± 0.83, 4.09 ± 1.07, and 5.48 ± 1.08 µm ($n = 109$ beads) (mean ± standard deviation, Fig. 1h). Representative imaging results of a CUBIC-cleared mouse brain labeled with brain-wide arterial (αSMA) and nuclear (SYTOX-G) stains are shown in Fig. 1i–k (Supplementary Video 2). The entire intact specimen is rapidly imaged with near-isotropic resolution using the mesoscopic ODO path of the hybrid system, which clearly resolves vasculature in all three dimensions. Detailed interrogation of a sub-region with the high-resolution NODO path resolves individual smooth muscle cells and sub-nuclear features, which are not resolved in ODO images of the same sub-region. We further

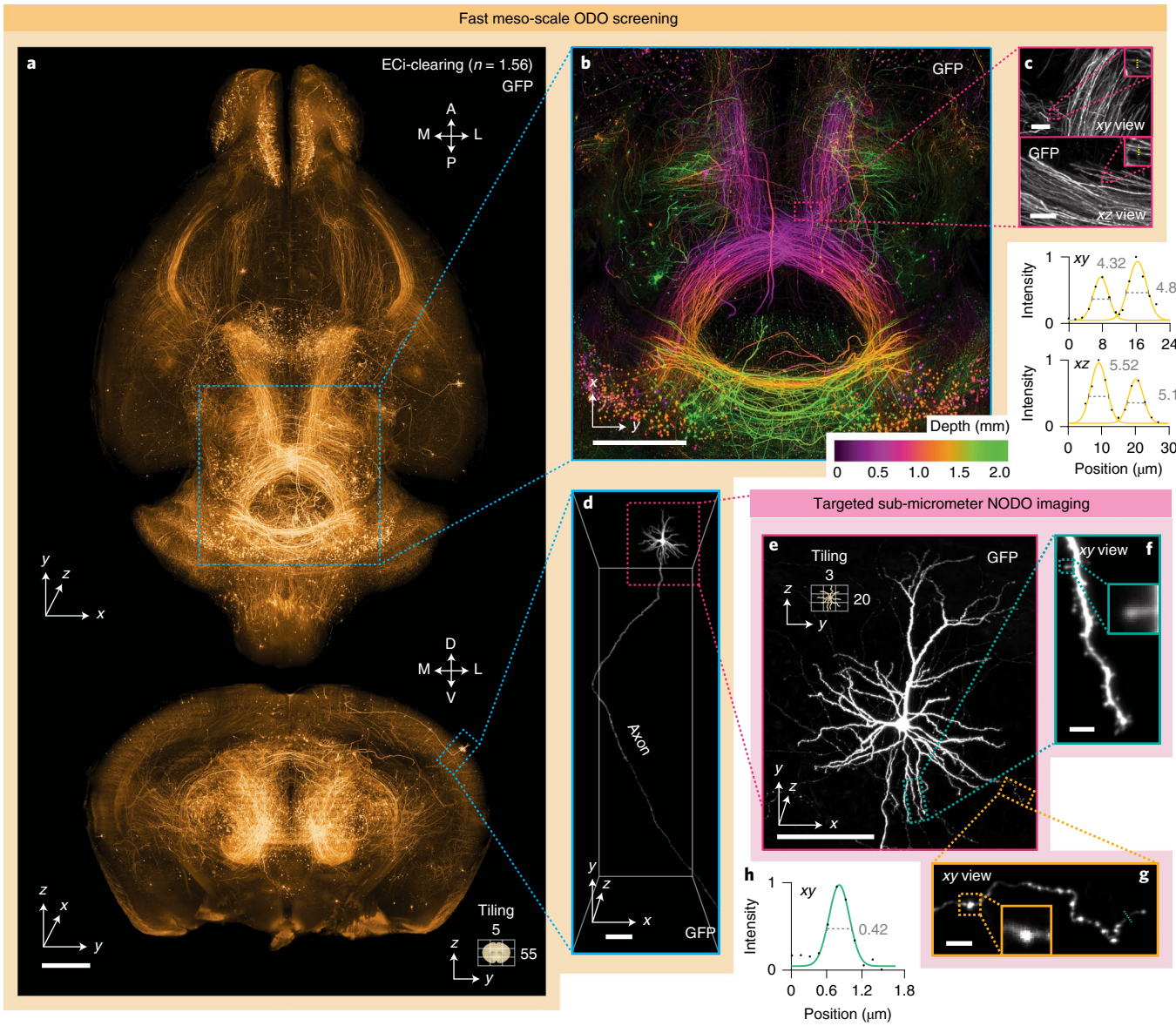

Fig. 2 | Fast meso-scale screening and targeted sub-micrometer imaging in cleared tissues. a, Fast meso-scale screening is performed of an entire intact ECi-cleared Slc17a7-Cre mouse brain with brain-wide axonal projections. **b**, A depth-coded region of interest shows dense projections in the midbrain. **c**, *xy* and *xz* zoom-in views illustrate the near-isotropic resolution of the hybrid OTLS microscope. Line profiles through individual axons demonstrate an ODO lateral and axial resolution of 4–5 μm at a large depth within the cleared specimen. **d**,**e**, Targeted sub-micrometer imaging is performed of a region of interest around a cortical pyramidal neuron. **f**,**g**, Zoom-ins of a dendrite and axon demonstrate sufficient lateral resolution to visualize individual spines and varicosities. **h**, A line profile through an individual axon demonstrates a NODO lateral resolution of 0.42 μm within the cleared specimen. Scale-bar lengths are as follows: **a**,**b**, 1 mm; **c**, 10 μm; **d**,**e**, 100 μm; and **f**,**g**, 5 μm. All images are displayed without deconvolution. The imaging data in **a**–**g** were acquired from a single mouse brain in a single experiment.

spotlight the unique utility of our hybrid system in two example applications in which multi-scale imaging enables time- and data-efficient experimental workflows.

Targeted imaging of sparse axons. First, we imaged axons in an intact mouse brain cleared in ethyl cinnamate (ECi) (Supplementary Video 3). Tracking the axons of individual neurons is a challenging problem—axons can be very thin (100 nm) and span very large distances (centimeters). To do this effectively, researchers typically rely on sparse and bright labeling of a few neurons along with high-resolution, high-contrast imaging of the entire brain (~0.5 cm^3)[40,41]. Sub-micrometer imaging of such large volumes generates datasets that are tens of terabytes in size, necessitating computationally intensive downstream pipelines for data handling, processing, and storage. The multi-scale imaging capability of our hybrid system accelerates and simplifies this process by screening an entire brain at low resolution to identify target regions with imageable neurons, followed by high-resolution imaging of the identified regions of interest.

Using the ODO imaging path, a mouse brain was rapidly screened in ~1 hour with isotropic ~2-μm voxels (~4-μm resolution), revealing brain-wide axonal projections (Fig. 2a,b). Inspection of dense axonal projections in *xy* and *xz* planes through the midbrain confirms the ability of the system to provide near-isotropic 4- to 5-μm resolution throughout the entire intact brain (Fig. 2c). A targeted region of interest around a cortical pyramidal neuron was then

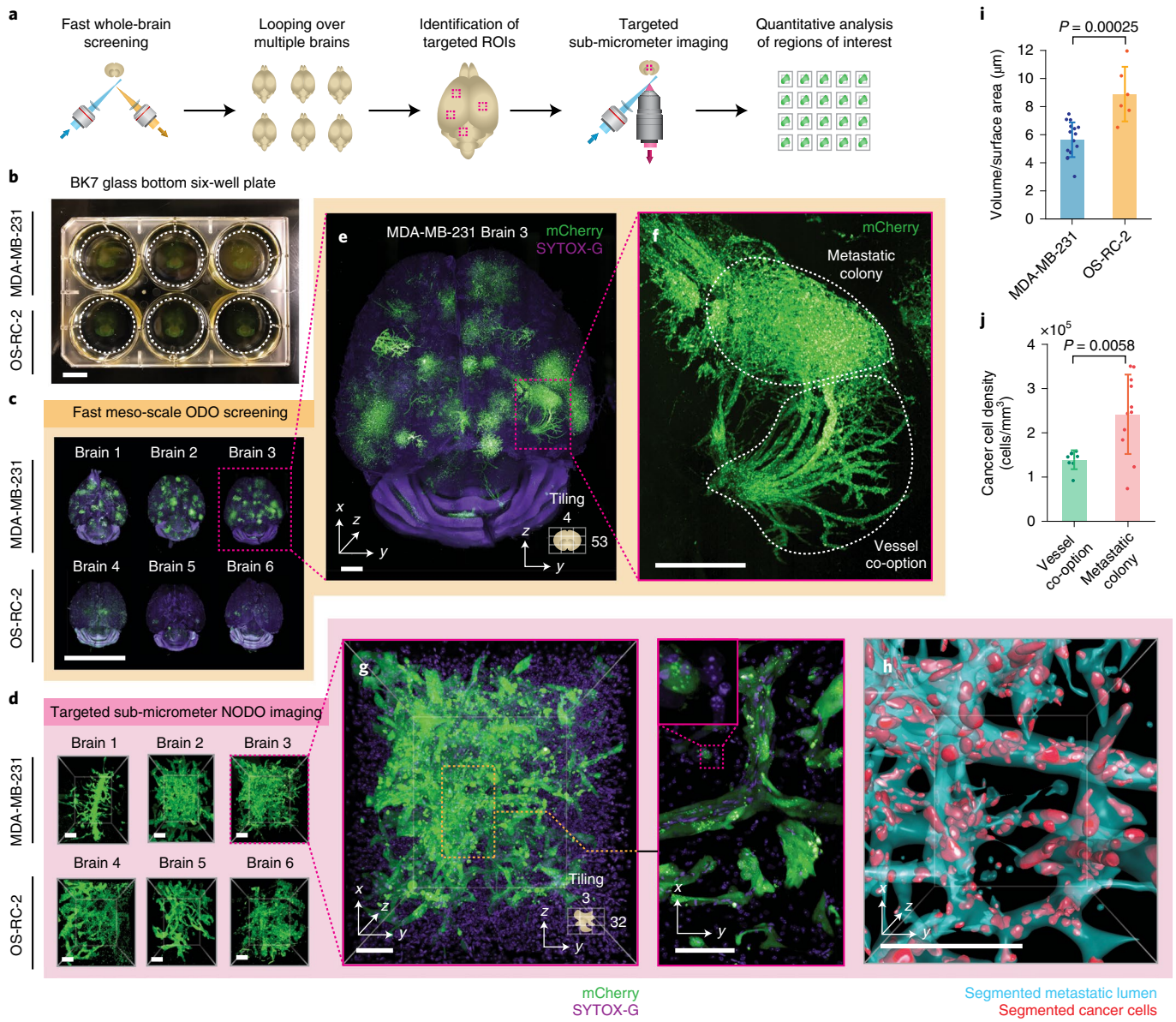

Fig. 3 | Multi-scale OTLS microscopy for quantitative analysis of brain metastases. a, Hybrid OTLS microscopy workflow for multi-scale imaging of multiple specimens. **b**, $n = 6$ whole mouse brains containing metastatic lesions from two different cancer cell lines (MDA-MB-231 and OS-RC-2) were placed into a glass-bottom 6-well plate and mounted onto the hybrid OTLS microscope system for multi-scale imaging. **c**, The ODO imaging path was used to rapidly screen multiple intact mouse brains containing metastatic colonies. **d**, $n = 34$ total metastatic ROIs across all brains were identified and subsequently imaged at sub-micrometer resolution using the NODO imaging path (only one ROI per brain is shown for illustrative purposes). **e**–**g**, Visual inspection of a single brain with MDA-MB-231 metastases in **e** revealed multiple colonies distributed throughout the brain, with signs of vessel co-option (**f**,**g**) that were not observed for OS-RC-2 metastases. **h**, To quantify these phenotypic differences between the MDA-MB-231 and OS-RC-2 metastases, the lumens spaces within the metastatic regions (cyan) and cancer cells (red) were computationally segmented and analyzed. **i**, The volume to surface area ratio was computed for MDA-MB-231 ROIs ($n = 16$) and OS-RC-2 ROIs ($n = 6$). Quantification of the resulting segmentation masks revealed statistically different 3D growth patterns (P value = 0.00025) between the two cancer cell lines, consistent with a previous report (**i**,**j**)[42]. **j**, For MDA-MB-231 ROIs, the cancer cell density in ROIs of metastatic colonies ($n = 11$) and vessel co-option ($n = 8$) was found to be statistically different ($P = 0.0058$). The center line and error bars in **i** and **j** denote the mean and s.d., with the associated data points plotted. P values in **i** and **j** were calculated using a two-sample t-test. Scale-bar lengths are as follows: **b**,**c**, 1 cm; **d**, 100 μm; **e**, 1 mm; **f**, 500 μm; **g**,**h**, 100 μm. All images are displayed without deconvolution. The imaging data in **c** were acquired from in a single experiment.

imaged at <0.5-μm xy resolution using the NODO imaging path (Fig. 2d,e). This imaging resolution is sufficient to discern spines and varicosities on individual dendrites and axons (Fig. 2f–h). Importantly, imaging a ~0.5-mm^3 sub-region containing the targeted neuron at ~0.5 × 0.5 × 2.7 μm (xyz) resolution required only 24 minutes, generating a 180-GB data set. By comparison, imaging the entire 0.5-cm^3 brain volume at this resolution would require >2 weeks of imaging and would produce >200 TB of imaging data.

Multi-scale imaging of metastatic colonies. In a second example, an imaging experiment was performed that required broad multi-scale imaging across multiple specimens. We used our hybrid

OTLS system to study metastatic colonies from two cancer cell lines (MDA-MB-231 and OS-RC-2) throughout intact mouse brains (Supplementary Video 4). Owing to the sparse and unpredictable spatial distribution of brain metastases, identifying those sites in whole brains is challenging without a rapid low-resolution screening method. Once metastatic sites are identified, high-resolution quantitative analysis of these regions is also desired. Whereas past studies have relied on manual transfer of individual specimens between different microscope systems[42] (for low-resolution localization followed by high-resolution analysis), we analyzed six intact mouse brains with our hybrid system in a single imaging session (Fig. 3a). While using a single system results in a lower duty cycle for each imaging mode (low-resolution and high-resolution imaging cannot be performed at the same time), consolidating two systems into a single hybrid system reduces overall hardware costs, simplifies the co-registration of multi-scale datasets, and helps automate multi-scale imaging experiments by obviating the need for manual transfer of specimens between different imaging systems.

All mouse brains were first placed in a standard 6-well plate (Fig. 3b) and screened sequentially using fast mesoscopic ODO imaging (Fig. 3c). After imaging, $n = 34$ total regions of interest (ROIs) centered on metastatic colonies were manually identified across all mouse brains and sequentially imaged without having to move the specimens or specimen holder. An example ROI from each brain is shown in Fig. 3d, with all 34 ROIs shown in Extended Data Fig. 1. Visual inspection of whole-brain images reveals that metastatic growth from MDA-MB-231 cancer cells exhibits vessel co-option (Fig. 3e–g), whereas OS-RC-2cancer cell metastases do not. Morphological analysis of volumetrically segmented brain metastases, performed across the high-resolution ROIs, reveal statistically significant differences between the two metastatic cell lines. For example, the 'volume-to-surface area ratio,' which correlates with the roundness of a metastatic colony, was found to be higher for the OS-RC-2 cell line (Fig. 3i). In addition, for the MDA-MB-231 cancer cell line, the density of cancer cells in the vessel co-option ROIs was found to be lower than the adjacent metastatic colonies (Fig. 3j). Both of these findings are consistent with the previous report from Kubota et al.[42]. However, this previous study required two separate microscope systems and several weeks of tedious imaging, including manual specimen transfer and co-registration of coordinates (personal correspondence with S. I. K.), whereas our hybrid OTLS system allowed the entire imaging experiment to be completed in ~2 days (~3–4 hours of low-resolution imaging time per whole brain and ~40–50 minutes of high-resolution imaging time per ROI).

Additional imaging examples. In addition to the examples shown, the system is well-equipped for an array of additional imaging experiments. These include: multi-scale non-destructive 3D pathology of prostate cancer with ECi clearing (Extended Data Fig. 2), whole brain imaging of endogenous fluorescent proteins with PEGASOS clearing (Supplementary Fig. 19 and Supplementary Video 5), 3D imaging of mouse embryos with SHIELD clearing (Supplementary Fig. 20), mapping of immune cell populations in 3D with Ce3D clearing (Supplementary Fig. 21 and Supplementary Video 6), assessment of 3D cell proliferation with iDISCO clearing (Extended Data Fig. 3 and Supplementary Video 7), imaging of plants/pigmented animal models processed with ClearSee/DEEP-Clear (Extended Data Fig. 4), screening of immunofluorescent and endogenously fluorescent mouse brains with CUBIC clearing (Extended Data Fig. 5 and Supplementary Videos 7–9), and large-scale imaging of amyloid plaques in thick human brain slices measuring up to 12 × 7.5 × 1 cm in size (Extended Data Fig. 6 and Supplementary Video 10).

As with all light-sheet microscopes, it is important to understand the various factors (for example system design, sample preparation, and sample mounting) that can have a major impact on image quality. We have summarized some of these considerations for potential users in Supplementary Note 4, with example imaging results at various depths for specimens cleared using CUBIC, PEGASOS, and ECi shown in Extended Data Figs. 7–9.

Discussion

In the future, both the axial and lateral resolution of the hybrid OTLS system can be improved. For example, the axial resolution of the system can be enhanced by incorporating a Bessel beam or by using a higher-NA Gaussian beam for light-sheet illumination[43] (Supplementary Fig. 21). This is facilitated by the fact that, unlike single-objective light-sheet systems, our new NODO architecture allows the illumination NA to be substantially increased without necessitating a concomitant decrease in the collection NA (that is, decoupled optical paths as shown in Fig. 1d). Similarly, axial sweeping could be incorporated into the system to reduce the number of vertical tiles and downstream computational burden for image stitching[16,17,44]. Although the current system contains an electronically tunable lens (ETL), we decided not to use the ETL for axial sweeping, as the ETL would limit the system's imaging speed. However, alternative devices, such as high-speed voice-coil actuators and tunable mirrors, could be incorporated in the future. With the 45-degree orientation of the two low-NA objectives in our system (one on either side of the NODO collection objective), it may also be possible to perform dual-sided illumination with fusion deconvolution to achieve improved image quality. However, this will not produce isotropic resolution since the crossing angle is not orthogonal (Supplementary Fig. 22)[19,36,45]. The lateral resolution of the system can be improved by increasing the collection NA of the multi-immersion objective. However, the optical cone angle cannot be increased beyond 40–45 degrees for a hybrid NODO–ODO system, as this would prevent the ODO objectives from being positioned at 45 degrees with respect to the vertical axis.

Although our current design uses three separate objectives, it is theoretically possible to achieve improved performance with an optimized NODO objective (Supplementary Fig. 23), or to achieve similar multi-scale OTLS performance using a single high-NA objective with a large FOV and working distance (see Supplementary Note 5 and Supplementary Fig. 24). For example, the pupil of a single objective could be split into three separate regions, using the edges for NODO illumination and for mesoscopic ODO imaging, and only the center for high-resolution NODO collection. However, this would require an objective with extraordinary specifications that could be prohibitively expensive to design and manufacture. Therefore, in summary, our hybrid OTLS design represents a practical means, with commercially available optical components, of achieving an impressive balance of performance and versatility in a single system for a growing number of cleared-tissue imaging experiments in which rapid low-resolution screening of large volumes is desired in addition to high-resolution characterization of localized subregions.

Online content

Any methods, additional references, Nature Research reporting summaries, source data, extended data, supplementary information, acknowledgements, peer review information; details of author contributions and competing interests; and statements of data and code availability are available at https://doi.org/10.1038/s41592-022-01468-5.

Received: 30 August 2021; Accepted: 24 March 2022;
Published online: 11 May 2022

References

1. Chung, K. et al. Structural and molecular interrogation of intact biological systems. *Nature* **497**, 332–337 (2013).

2. Tanaka, N. et al. Whole-tissue biopsy phenotyping of three-dimensional tumours reveals patterns of cancer heterogeneity. *Nat. Biomed. Eng.* **1**, 796 (2017).
3. Richardson, D. S. & Lichtman, J. W. Clarifying tissue clearing. *Cell* **162**, 246–257 (2015).
4. Pan, C. et al. Shrinkage-mediated imaging of entire organs and organisms using uDISCO. *Nat. Methods* **13**, 859–867 (2016).
5. Renier, N. et al. iDISCO: a simple, rapid method to immunolabel large tissue samples for volume imaging. *Cell* **159**, 896–910 (2014).
6. Tainaka, K. et al. Chemical landscape for tissue clearing based on hydrophilic reagents. *Cell Rep.* **24**, 2196–2210.e9 (2018).
7. Susaki, E. A. et al. Advanced CUBIC protocols for whole-brain and whole-body clearing and imaging. *Nat. Protoc.* **10**, 1709–1727 (2015).
8. Chung, K. & Deisseroth, K. CLARITY for mapping the nervous system. *Nat. Methods* **10**, 508–513 (2013).
9. Susaki, E. A. et al. Versatile whole-organ/body staining and imaging based on electrolyte-gel properties of biological tissues. *Nat. Commun.* **11**, 1982 (2020).
10. Jing, D. et al. Tissue clearing of both hard and soft tissue organs with the PEGASOS method. *Cell Res.* **28**, 803–818 (2018).
11. Power, R. M. & Huisken, J. A guide to light-sheet fluorescence microscopy for multiscale imaging. *Nat. Methods* **14**, 360 (2017).
12. Huisken, J. & Stainier, D. Y. R. Selective plane illumination microscopy techniques in developmental biology *Development* **136**, 1963–1975 (2009).
13. Dodt, H.-U. et al. Ultramicroscopy: three-dimensional visualization of neuronal networks in the whole mouse brain. *Nat. Methods* **4**, 331–336 (2007).
14. Migliori, B. et al. Light sheet theta microscopy for rapid high-resolution imaging of large biological samples. *BMC Biol.* **16**, 57 (2018).
15. Tomer, R. et al. Advanced CLARITY for rapid and high-resolution imaging of intact tissues. *Nat. Protoc.* **9**, 1682–1697 (2014).
16. Voigt, F. F. et al. The mesoSPIM initiative: open-source light-sheet microscopes for imaging cleared tissue. *Nat. Methods* **16**, 1105–1108 (2019).
17. Chakraborty, T. et al. Light-sheet microscopy of cleared tissues with isotropic, subcellular resolution. *Nat. Methods* **16**, 1109–1113 (2019).
18. Chen, Y. et al. A versatile tiling light sheet microscope for imaging of cleared tissues. *Cell Rep.* **33**, 108349 (2020).
19. Kumar, A. et al. Dual-view plane illumination microscopy for rapid and spatially isotropic imaging. *Nat. Protoc.* **9**, 2555–2573 (2014).
20. Strnad, P. et al. Inverted light-sheet microscope for imaging mouse pre-implantation development. *Nat. Methods* **13**, 139–142 (2015).
21. McGorty, R. et al. Open-top selective plane illumination microscope for conventionally mounted specimens. *Opt. Express* **23**, 16142–16153 (2015).
22. McGorty, R., Xie, D. & Huang, B. High-NA open-top selective-plane illumination microscopy for biological imaging. *Opt. Express* **25**, 17798–17810 (2017).
23. Glaser, A. K. et al. Light-sheet microscopy for slide-free non-destructive pathology of large clinical specimens. *Nat. Biomed. Eng.* **1**, 0084 (2017).
24. Glaser, A. K. et al. Multi-immersion open-top light-sheet microscope for high-throughput imaging of cleared tissues. *Nat. Commun.* **10**, 1–8 (2019).
25. Barner, L. A. et al. Solid immersion meniscus lens (SIMlens) for open-top light-sheet microscopy. *Opt. Lett.* **44**, 4451–4454 (2019).
26. Barner, L. A. et al. Multi-resolution open-top light-sheet microscopy to enable efficient 3D pathology workflows. *Biomed. Opt. Express* **11**, 6605–6619 (2020).
27. Botcherby, E. J. et al. An optical technique for remote focusing in microscopy. *Opt. Commun.* **281**, 880–887 (2008).
28. Dunsby, C. Optically sectioned imaging by oblique plane microscopy. *Opt. Express* **16**, 20306–20316 (2008).
29. Voleti, V. et al. Real-time volumetric microscopy of in vivo dynamics and large-scale samples with SCAPE 2.0. *Nat. Methods* **16**, 1054–1062 (2019).
30. Bouchard, M. B. et al. Swept confocally-aligned planar excitation (SCAPE) microscopy for high-speed volumetric imaging of behaving organisms. *Nat. Photonics* **9**, 113–119 (2015).
31. Yang, B. et al. Epi-illumination SPIM for volumetric imaging with high spatial-temporal resolution. *Nat. Methods* **16**, 501–504 (2019).
32. Millett-Sikking, A. et al. High NA single-objective light-sheet. https://andrewgyork.github.io/high_na_single_objective_lightsheet/index.html (2019).
33. Kumar, M. et al. Integrated one- and two-photon scanned oblique plane illumination (SOPi) microscopy for rapid volumetric imaging. *Opt. Express* **26**, 13027–13041 (2018).
34. Hoffmann, M. & Judkewitz, B. Diffractive oblique plane microscopy. *Optica* **6**, 5 (2019).
35. Sapoznik, E. et al. A versatile oblique plane microscope for large-scale and high-resolution imaging of subcellular dynamics. *eLife* **9**, e57681 (2020).
36. Yang, B. et al. DaXi-high-resolution, large imaging volume and multi-view single-objective light-sheet microscopy. *Nat. Methods* **19**, 461–469 (2022).
37. Li, T. et al. Axial plane optical microscopy. *Sci. Rep.* **4**, 7253 (2014).
38. Kim, J. et al. Oblique-plane single-molecule localization microscopy for tissues and small intact animals. *Nat. Methods* **16**, 853–857 (2019).
39. Bishop, K. W., Glaser, A. K. & Liu, J. T. C. Performance tradeoffs for single- and dual-objective open-top light-sheet microscope designs: a simulation-based analysis. *Biomed. Opt. Express* **11**, 4627–4650 (2020).
40. Economo, M. N. et al. A platform for brain-wide imaging and reconstruction of individual neurons. *eLife* **5**, e10566 (2016).
41. Winnubst, J. et al. Reconstruction of 1,000 projection neurons reveals new cell types and organization of long-range connectivity in the mouse brain. *Cell* **179**, 268–281.e13 (2019).
42. Kubota, S. I. et al. Whole-body profiling of cancer metastasis with single-cell resolution. *Cell Rep.* **20**, 236–250 (2017).
43. Planchon, T. A. et al. Rapid three-dimensional isotropic imaging of living cells using Bessel beam plane illumination. *Nat. Methods* **8**, 417–423 (2011).
44. Dean, K. et al. Deconvolution-free subcellular imaging with axially swept light sheet microscopy. *Biophys. J.* **108**, 2807–2815 (2015).
45. Sparks, H. et al. Dual-view oblique plane microscopy (dOPM). *Biomed. Opt. Express* **11**, 7204–7220 (2020).

Methods

Hybrid open-top light-sheet microscope. Light-sheet-based imaging is achieved using three optical arms. The first obliquely illuminates the specimen with a light sheet at 45 degrees relative to the vertical axis. The second is oriented vertically, enabling high-resolution collection of the light-sheet-generated fluorescence in a NODO configuration. Finally, the third arm is oriented at 90 degrees relative to the illumination light sheet, enabling high-speed mesoscopic imaging in an ODO configuration. All three objectives are positioned below the specimen and are sealed into a custom-designed monolithic imaging chamber (machined by Hilltop Technologies). In the case of each angled air objective, a custom-fabricated solid-immersion meniscus lens (SIMlens) (fabricated by BMV Optical Technologies) is sealed into the chamber (Supplementary Fig. 6)[25]. Stage-scanning is achieved by using an *XY* stage (MS2000, Applied Scientific Instrumentation) attached to two *Z*-axis risers (LS50, Applied Scientific Instrumentation). Laser-light excitation at 405, 488, 561, and 638 nm is provided to the illumination path by a multi-line laser package (Cobolt Skyra, HÜBNER Photonics). The NODO collection path is equipped with a motorized filter wheel (FW102C, Thorlabs) with 4 filters that can be used with 405-nm (FF02-447/60-25, Semrock), 488-nm (FF03-525/50-25, Semrock), 561-nm (FF01-618/50-25, Semrock), or 638-nm (BLP01-647R-25, Semrock) excitation. The ODO collection path is equipped with a single multi-band-pass filter (FF01-432/515/595/730-25, Semrock) that can be used with any of the four excitation wavelengths. The entire system is compact and fits on a portable 2′ × 3′ optical cart (POC001, Thorlabs).

Illumination optical path. The illumination optical arm is shown in Supplementary Fig. 10. The illumination optics are designed to allow for the light-sheet properties (that is, width, thickness, and depth of focus) to be adjusted. In addition, the optical path is designed to be compatible with the refractive index, *n*, of all current clearing protocols (that is, it has multi-immersion capabilities) and to minimize chromatic aberrations and defocusing (that is, variations in the illumination focal length as a function of wavelength).

Illumination light is fiber coupled into the system with a Gaussian numerical aperture (NA) of ~0.12 and collimated using an objective (RMS20×, Olympus). The beam diameter is then adjusted using a ×4 variable beam expander (BE052-A, Thorlabs). This serves to adjust the overall NA of the light sheet. The variably expanded beam is then passed through an electronically tunable lens (ETL) that enables axial adjustment/alignment of the light sheet (EL-16-40-TC-VIS-5D-C, Optotune). The axially adjusted beam is relayed 1:1 using a pair of lenses (AC254-75A, Thorlabs) so that it can be scanned using a pair of large-beam-diameter galvanometric scanning mirrors (GVS012, Thorlabs). One mirror is scanned to create a digitally scanned light sheet[46]. The other scanning mirror is used to align the light sheet with the focal plane of the NODO and ODO imaging paths. A pair of achromatic doublet lenses (AC508-75A and AC508-200A, Thorlabs) are then used to relay the scanned beam to the back focal plane of a ×2 illumination objective with NA = 0.10 (TL2X-SAP, Thorlabs). Finally, the illumination light travels through the SIMlens (Supplementary Fig. 6)[25]. The SIMlens provides multi-immersion performance and prevents aberrations (spherical, off-axis, and chromatic) of the light sheet by minimizing refraction of the illumination rays as they transition from air into the immersion medium. In addition, since ray angles are preserved as they transition between air and the immersion medium, the SIMlens increases the NA of the illumination light sheet by a factor of *n*. When combined, this optical design yields a light sheet with tunable NA (0.025–0.10 × *n*) and tunable width (0–11 mm / *n*), limited by FOV of the illumination objective.

A digitally scanned light sheet was chosen over a cylindrical-lens approach (static light sheet), as this facilitates achieving a high level of tunability for multi-scale imaging. Moreover, large scanning mirrors were selected to fill the back focal plane of the final illumination objective and to avoid having to significantly magnify the beam after the scanning mirrors, which would reduce the lateral scanning range of the mirrors (that is, constrain the maximum light-sheet width). In the current design, rotating the scanning mirror results in lateral scanning at a ratio of ~0.60 mm per degree / *n*. The maximum desired light sheet width (that is, lateral scanning range) is 11 mm, corresponding to a scanning angle of ~18 degrees, which is within the maximum scan range of the galvo scanner (20 degrees).

NODO optical path. The physical layout, ZEMAX model, and objective options for this NA-maximized NODO imaging configuration are shown in Supplementary Fig. 11. The NODO optical path of our system uses a multi-immersion objective (no. 54-12-8, Special Optics) with a long 1-cm working distance. This objective is compatible with all clearing protocols (*n* = 1.33–1.56) and provides a NA of 0.483 (in air) that scales with the index of the immersion medium (for example, NA ~ 0.75 at *n* = 1.56). The lens is oriented in the normal (vertical) direction with respect to the specimen holder/interface and is therefore non-orthogonal to the light sheet. To image this non-orthogonal light sheet, we use a remote focus imaging strategy analogous to what is used for single-objective light-sheet systems, with the multi-immersion objective serving as the primary objective (O1)[27,28].

To minimize aberrations in the remote focus relay, the overall magnification from the specimen to the remote focus (air) should be equal to the refractive index of the specimen, *n*. Given this requirement, the relay lenses and first remote objective (O2) must be carefully selected. For O2, a ×20 objective is optimal, as a ×10 or ×40 objective would clip either the NA or FOV of our O1. Of the several companies that produce microscope objectives, Zeiss and Leica were avoided because chromatic aberrations are partially corrected in the tube lenses produced by these companies, which would complicate selection of the two relay tube lenses. Therefore, only objectives from Olympus and Nikon were considered: ×20 objectives from Olympus have a focal length of 9 mm, and ×20 objectives from Nikon have a focal length of 10 mm. Factoring in the effective focal length of O1 (12.19 mm / *n*), the required relay lens magnification is ~×1.219 for Nikon and ~×1.354 for Olympus. Note that the magnification of the multi-immersion objective in our system scales inversely as a function of *n*. This allows us to use a fixed set of relay lenses and to always satisfy the remote focusing magnification requirement. However, this would be problematic with alternative multi-immersion objectives, where the effective focal length does not vary with *n*, and therefore the magnification of the relay lenses would need to be adapted for each immersion medium.

Well-corrected tube lenses are available with a limited selection of focal lengths (100, 165, 180, and 200 mm). Although custom tube lens assemblies are possible[32], we found that off-the-shelf 200-mm (Nikon Tube Lens no. 58-520, Edmund Optics) and 165-mm (TTL165-A, Thorlabs) tube lenses provide a magnification of ~×1.212, which matches the requirement for Nikon. Therefore, we decided to select a ×20 Nikon objective for O2. To avoid the need for a cover glass, we narrowed our selection to Nikon objectives designed for use without a cover glass. This yielded one option, the LU (now TU) Plan Fluor EPI ×20 (NA = 0.45). We chose this objective for the O2 in the current system.

To remotely correct for spherical aberrations introduced by the index mismatch of the specimen holder, it would also be possible to use a Nikon objective with a correction collar. There are two options, the CFI S Plan Fluor ELWD 20XC (NA = 0.45) with a correction collar for a cover glass of thickness, *t* = 0–2 mm, and CFI S Plan Fluor LWD 20XC (NA = 0.70) with a correction collar for a cover glass of *t* = 0 – 1.8 mm. Both objectives could be explored in a future design (although spherical aberrations were not found to be an issue in the current design). In the case of the CFI S Plan Fluor LWD 20XC, the full 0.483 NA of our O1 objective could be transmitted to the remote focus, unlike the chosen LU Plan Fluor EPI ×20 objective or CFI S Plan Fluor ELWD 20XC objective, which both clip things down to 0.45 NA.

The goal of O3 is to maximize light collection when tilted at the angle required to orthogonally image a remote version of the oblique light sheet within the specimen. As mentioned previously, in a single-objective light-sheet design, the light-sheet angle would be limited by our chosen O1 to a maximum of 28.9 degrees. This would require O3 to be tilted by at least 61.1 degrees. At this extreme tilt angle, one way to prevent light loss is through a custom solid- or liquid-immersion objective[31,32]. However, a benefit of our NODO design is that the crossing angle can be increased to 45 degrees, which reduces the tilt of O3 to 45 degrees. At this tilt angle, an objective with NA = 0.95 is able to capture light up to NA = 0.45 and provide NA-maximized imaging. Therefore, we opted to use a NA = 0.95 air objective for our O3. This use of a tertiary air objective makes alignment more straightforward and stable than in the case of a solid- or liquid-immersion objective[31,32]. This is especially the case for liquid-immersion objectives, where there may be evaporation or leakage of a liquid medium over time.

In terms of selecting an optimal O3 for NA-maximized imaging, we considered only objectives from Olympus and Nikon for the same reasons as mentioned previously. Both companies offer two types of objectives with NA = 0.95. These include ×40 life-science objectives with a correction collar for cover-glass thicknesses ranging from *t* = 0.11–0.23 mm, and ×50 metrology objectives for imaging with no cover glass. Although it would be possible to permanently align or adhere a cover glass to the ×40 objectives, we decided to select the CF IC EPI Plan Apo ×50 objective from Nikon for our O3 for simplicity and ease of use. When combined with a 100-mm tube lens (TTL100-A, Thorlabs), our NODO imaging path provides a total magnification of 25 × *n*. This yields a sampling rate of ~2.71 (slightly better than Nyquist) when using a sCMOS camera with pixels spaced by 6.5 µm (pco.edge 4.1, PCO Tech). The corresponding FOV is ~0.53 mm / *n* (FOV = 0.40–0.34 mm when *n* = 1.33–1.56), which is not clipped by the 0.40-mm FOV of the ×50 objective. In this configuration, the back aperture of the illumination objective is filled, yielding an illumination NA of ~0.10 × *n*. This corresponds to a beam waist of ~2–3 µm and confocal parameter of ~40–50 µm (corresponding to a pixel height of ~256 pixels for each raw camera image) depending on the illumination wavelength and immersion medium. This also corresponds to an axial re-focusing range that is well within the range of operation for an idealized objective, as specified by Botcherby et al.[27]. The pixel width of each raw camera frame is the full 2,048 pixels of the sCMOS camera, corresponding to a FOV of ~0.34–0.40 mm.

While the above O3 selection provides NA-maximized imaging, our O1 also provides a 1-mm FOV to enable FOV-maximized imaging (with slightly worse resolution). To achieve this, O3 can be changed to a ×20 objective with a matched 1-mm FOV. To minimize light loss, ×20 objectives with the highest NA were considered. For both Olympus and Nikon, the upper limit is NA = 0.75 (although the recent UPLXAPO20X objective from Olympus offers NA = 0.80). In a single-objective light-sheet configuration, the light sheet angle in the specimen would be limited by the NA of O1, requiring a larger remote tilt angle, which for

this particular O3 would result in an effective NA ~ 0.12 × *n*. In contrast, with our NODO configuration, this results in an effective NA of ~ 0.26 × *n*. This reduced effective NA (in contrast to the NA-maximized case) enables close-to-Nyquist sampling of a 1-mm FOV with the same sCMOS chip as described earlier (with 2048 × 2048 pixels). To match parfocal lengths and thus enable a quick interchange of objectives, we selected the Nikon CFI Plan Apo Lambda ×20 for our FOV-maximized O3 objective. When paired with the same 100-mm tube lens (TTL100-A, Thorlabs), this provides a total magnification of 10 × *n*, which yields a near-Nyquist sampling rate of 2.02. The effective FOV is ~ 1.33 mm / *n* (FOV = 1.00–0.85 mm when *n* = 1.33–1.56), which is not clipped by the 1.00 mm FOV of the ×20 objective (O3). The physical layout, ZEMAX model, and objective options for this FOV-maximized NODO imaging configuration are shown in Supplementary Fig. 12. See Supplementary Note 3 for more discussion of NA- versus FOV-maximized imaging. As mentioned previously, an alternative design could use the CFI S Plan Fluor LWD 20XC and a customized O3 to make use of the full 0.483 NA of our O1 (see Supplementary Fig. 13 and Supplementary Note 6).

The NODO path of the hybrid system contains multiple additional lenses (compared with the collection path of a traditional light-sheet system). These additional components reduce the overall light throughput of the optical path. To characterize the reduction in light collection efficiency introduced by remote refocusing, laser light at 405, 488, 561, and 638 nm was focused through the primary objective lens (O1) of the system. The light was transmitted through the entire NODO optical path (O1, TL1, TL2, O2, O3, and TL3) and the transmitted power was measured after the final tube lens (TL3) at the position of the camera. The light throughput was compared with the transmitted power at the intermediate image plane between TL1 and TL2 (where the camera would be positioned for a traditional light-sheet system). The light collection efficiency was measured to be 50% at 405 nm, 72% at 488 nm, 76% at 561 nm, and 70% at 638 nm.

ODO optical path. The physical layouts and ZEMAX models of the ODO imaging configurations are shown in Supplementary Fig. 14–15. While the NODO imaging path can provide sub-micrometer resolution, the FOV of the multi-immersion primary objective (O1) is restricted to 1 mm, which is insufficient for fast mesoscopic imaging. This tradeoff between NA and FOV is standard across all currently available microscope objectives (for example, no current clearing-compatible objectives can simultaneously offer sub-micrometer resolution over a FOV of up to 1 cm) (Supplementary Fig. 8)[47]. Therefore, in our hybrid system, we achieve low-resolution imaging with a second independent ODO imaging path.

The ODO collection path uses the same objective as the illumination optical path (TL2X-SAP, Thorlabs). The objective is similarly used in conjunction with a SIMlens (fabricated by BMV Optical Technologies), which provides multi-immersion performance and prevents axial chromatic aberrations in the ODO imaging path[25]. In addition, the SIMlens increases the NA of the collection path by a factor of *n*. This yields an effective NA = 0.10 × *n*.

The current set point of the ODO collection path lies between the NA- and FOV-maximized imaging extremes and uses a tube lens with a 200-mm focal length (TTL200-A, Thorlabs). This provides a magnification of 2 × *n* and an effective FOV of 6.6 mm / *n*, which undersamples the collection NA of the system when using a sCMOS camera with a pixel spacing of 6.5 µm (pco.edge 4.1, PCO Tech, 2048 × 2048 pixels). In this configuration, the back aperture of the illumination objective is underfilled to yield an illumination NA of ~0.04 × *n*. This corresponds to a beam waist of ~4.5–6.5 µm and confocal parameter of ~250–300 µm (corresponding to a pixel height of ~128 pixels for each raw camera image) depending on the illumination wavelength and immersion medium. The width (in pixels) of each raw camera image is the full 2048 pixels of the sCMOS camera, corresponding to a distance of ~4.25–5 mm in the sample. This combination of illumination and collection NA provides near-isotropic resolution (Supplementary Fig. 17).

The magnification of the ODO imaging path is easily adjusted by changing the tube lens. NA-maximized imaging is achieved using a tube lens with a 400-mm focal length (AC508-400-A, Thorlabs). This provides a magnification of 4 × *n* and an effective FOV of 3.3 mm / *n*, which corresponds to a near-Nyquist sampling rate of ~2.1 when using a sCMOS camera with a pixel spacing of 6.5 µm. FOV-maximized imaging is achieved using a tube lens with a 100-mm focal length (TTL100-A, Thorlabs). This provides a magnification of 1 x *n* and an effective FOV of 13.33 mm / *n*. See Supplementary Note 3 for more discussion of NA- versus FOV-maximized imaging modes.

Image acquisition and post-processing. Image strips are collected with a combination of stage-scanning and lateral/vertical tiling. The stage-scanning firmware is used to send a TTL SYNC trigger signal from the *XY* stage to the sCMOS camera for reproducible initiation of each imaging strip. After triggering, the camera is set to free-running mode and acquires the desired number of frames for a given image-strip length (as the sample is scanned by the stage at a constant velocity), with a spacing between adjacent frames that is identical to the sampling pitch of the raw camera images. For each raw frame, the camera uses the standard rolling shutter, where the shutter rolls from the center of the camera chip in both directions, as opposed to the light-sheet readout mode, where the shutter rolls from the top to the bottom of the camera chip. Using the standard rolling shutter, the rolling directions are oriented along the light sheet propagation direction. This orientation allows the imaging speed to be increased when the pixel height of each raw frame is cropped to match the confocal parameter of the illumination light sheet.

At the start of each exposure, the camera sends a trigger to an analog output DAQ card (PCIe-6738, National Instruments). The DAQ card then sends output voltages to the lasers, galvos, and ETL (for alignment only, not axial sweeping). To reduce motion blur, the lasers and galvos are triggered with a delay to illuminate only once the shutter has rolled across the full pixel height of the camera frame, resulting in a strobing effect. For the 128- or 256-pixel height of the ODO and NODO paths, respectively, the rolling time, t_{roll}, is 0.625 and 1.25 ms. The exposure time, t_{exp}, is set to 3 × t_{roll}, resulting in a total exposure time, t_{tot}, of 4 × t_{roll}, or 2.5 and 5 ms for the ODO and NODO paths. This corresponds to a data rate that is one-fourth the maximum data rate of the sCMOS camera. The lateral scanning mirror is actuated with a sawtooth waveform and completes a single period within the total exposure time, t_{tot}, of the raw camera frame, corresponding to a frequency of ~400 and ~200 Hz for the ODO and NODO paths. The ETL and second mirror are set to a pre-calibrated DC voltage for the entire image strip to yield an in-focus light sheet that is axially aligned to the center of the camera chip.

Raw camera frames are streamed from the camera to RAM and subsequently saved directly as a single HDF5 file and XML file with the associated metadata, which is suitable for immediate processing with BigStitcher via ImageJ[48,49]. This involves on-the-fly saving of down-sampled copies of the image strip (×2, ×4, ×8, and ×16) in the hierarchical HDF5 file format. Additionally, the GPU-based B3D compression filter can be optionally added to the HDF5 writing process to yield 5–10× compression with negligible loss of usable information content[50]. However, both processing steps slow down the net data rate from RAM to disk. On-the-fly saving of down-sampled copies of the image strips slows the data rate by ~2×, and the B3D algorithm slows down the process by another ~2×. This net speed reduction of ~4× motivated our selection of the camera frame rate mentioned previously. For our experiments, these reductions in post-processing times and data-storage requirements are worth the reduction in imaging speed. However, it is important to note that the imaging speeds could be increased by 2× if the aforementioned processing steps are omitted from the acquisition procedure, in which case the imaging speed would become limited by the duty cycle of the illumination strobing, where $t_{exp} = t_{roll}$.

A ~15% overlap is used for both vertical and lateral tiling. Different wavelength channels are acquired sequentially. For each image strip 'tile' that is acquired by laterally scanning the specimen in the *y*-direction, all channels are acquired by cycling through various laser/filter combinations and re-scanning that image strip for each laser/filter setting, before moving to the next tile position. When tiling vertically, the laser power is increased with depth per a user-defined exponential relationship, $P = P_0 \times \exp(z / \mu)$, to account for the attenuation of the illumination light sheet as it penetrates deeper into the specimen (typically $\mu = 5–20\ mm^{-1}$). Finally, if desired, all of the imaging tiles can be aligned and fused into one contiguous 3D image as an HDF5 or TIFF file output using BigStitcher[48]. The entire image acquisition is controlled using a custom-written Python program that is available from the authors upon request.

Imaging speed. The volumetric imaging speed of the system depends on many factors, including the camera data rate, imaging path, magnification set point, tiling overlap, overall imaging volume, and timing delays intrinsic to the acquisition (for example, stage time to move to the next tile position). The imaging speeds shown in Fig. 1g were calculated on the basis of the actual operation of the microscope, assuming the camera is operating at 25% of the maximum data rate (~100 megavoxels/sec), a 15% overlap between adjacent tiles, and a stage velocity of 5 mm/sec when moving between successive tile positions. For the NODO path, a total imaging volume of ~1 mm^3 was assumed, corresponding to ~3 lateral tiles and 40 vertical tiles for the given magnification set point. For the ODO path, a total imaging volume of ~1 cm^3 was assumed, corresponding to ~3 lateral tiles and 66 vertical tiles for the given magnification set point.

Computer hardware. During acquisition, the images are collected by a dedicated custom workstation (Puget Systems) equipped with a high-specification motherboard (Asus WS C422 SAGE/10 G), processor (Intel Xeon W-2145 3.7 GHz 8 Core 11MB 140 W), and 256 GB of RAM. The motherboard houses several PCIe cards, including 2 CameraLink frame grabbers (mEIV AD4/VD4, Silicon Software) for streaming images from the camera, a DAQ card (PCIe-6738, National Instruments) for generating analog output voltages, a 10 G SFP + network card (StarTech), and a GPU (TitanXP, NVIDIA). Datasets are streamed to a local 8-TB U.2 drive (Micron) that is capable of outpacing the data rates of the microscope system. Data is then transferred to a mapped network drive located on an in-lab server (X11-DPG-QT, SuperMicro) running 64-bit Windows Server, equipped with 768 GB RAM and TitanXP (NVIDIA) and Quadro P6000 (NVIDIA) GPUs. The mapped network drive is a direct-attached RAID6 storage array with 15 × 8.0 TB HDDs. The RAID array is hardware based and controlled by an external 8-port controller (LSI MegaRaid 9380–8e 1 GB cache). Both the server and acquisition workstation are set with jumbo frames (Ethernet frame) and parallel send/receive

processes matched to the number of computing cores on the workstation (8 physical cores) and server (16 physical cores), which reliably enables ~1.0 GB/sec network-transfer speeds.

ECi-cleared mouse brain. Labeling and clearing were carried out as previously described[41]. For sparse labeling, a Slc17a7-Cre mouse (female, 8 weeks old) received a systemic injection, via the retro-orbital sinus, of a mixture of Cre-dependent Tet transactivator (PHP-eB-Syn-Flex-TRE-2×-tTA) and a reporter virus (PHP-eB-CAG-TRE-3×GFP)[41,51]. High-titer (>10^{12} GC/mL) viruses were obtained from the Janelia Research Campus Molecular Biology Core and diluted in sterile water when necessary.

Transfected mice were anesthetized with an overdose of isoflurane and then transcardially perfused with a solution of PBS containing 20 µg/mL heparin (Sigma-Aldrich no. H3393) followed by a 4% paraformaldehyde solution in PBS. Brains were extracted and post-fixed in 4% paraformaldehyde at 4 °C overnight (12–14 hours) and washed in PBS to remove all traces of excess fixative (PBS changes were performed at 1 hours, 6 hours, 12 hours, and 1 day).

For amplification by immuno-labeling, brains were delipidated with a modified Adipo-Clear protocol[52]. Brains were washed with a methanol gradient series (20%, 40%, 60%, 80%, Fisher no. A412SK) in B1n buffer (H_2O/0.1% Triton X-100/0.3 M glycine, pH 7; 4 mL/brain; 1 hour/step). Brains were then immersed in 100% methanol for 1 hour, 100% dichloromethane (Sigma no. 270997) for 1.5 hours, and 3 times in 100% methanol for 1 hour. Samples were then treated with a reverse methanol gradient series (80%, 60%, 40%, 20%) in B1n buffer for 30 minutes at each step. All procedures were performed on ice. Samples were washed in B1n buffer for 1 hour and left overnight at room temperature and were then again washed in PTxwH buffer (PBS/0.1% Triton X-100/0.05% Tween 20/2 µg/mL heparin) with fresh solution after 1 and 2 hours and then were left overnight.

After delipidation, selected samples were incubated in primary antibody dilutions in PTxwH for 14 days on a shaker (1:1,000, anti-GFP, Abcam, no. ab290). Samples were sequentially washed in 25 mL PTxwH for 1, 2, 4, 8 hours, and 3 times for 24 hours. Samples were incubated in secondary antibody dilutions in PTxwH for 14 days (1:600, Alexa Fluor 488-conjugated donkey-anti-rabbit IgG) and washed in PTxwH, similar to what was described above. Finally, the tissue was dehydrated in ethanol grades (25%, 50%, 75%, 100%) for 8 hours per grade. The 100% grade was repeated to ensure removal of all water from the tissue. Finally, the tissue was cleared in ethyl cinnamate (Sigma-Aldrich no. 112372) for 8 hours before imaging. All experimental protocols were conducted according to the National Institutes of Health guidelines for animal research and were approved by the Institutional Animal Care and Use Committee at Howard Hughes Medical Institute, Janelia Research Campus.

MDA-MB-231/OS-RC-2 and αSMA-labeled mouse brains. Human breast cancer cells, MDA-MB-231-5a-D (MDA-MB-231) are highly metastatic clones from MDA-MB-231 (ref. [53]). Human renal cell carcinoma cells (OS-RC-2) were kindly provided by T. Irimura (Juntendo University, Japan). MDA-MB-231 cells were cultured in DMEM supplemented with 10% FBS, 100 U/ml penicillin and 100 µg/ml streptomycin as previously described[53]. OS-RC-2 cells were maintained in RPMI1640 containing 10% FBS and penicillin/streptomycin[54].

To establish cancer cells stably expressing firefly luciferase and mCherry under the EF-1 promoter, a lentiviral expression system was used (kindly provided by H. Miyoshi, deceased, formerly Keio University, Tokyo, Japan) as described previously[55]. Briefly, 293FT cells were transfected with a vector construct encoding the expression protein, VSV-G, a Rev-expressing construct (pCMV-VSV-G-RSV-Rev), and a packaging construct (pCAG-HIVgp). The culture supernatants containing viral particles were collected and used as lentiviral vectors.

BALB/c-nu/nu mice (female, 4 weeks old) were purchased from Japan SLC (Shizuoka, Japan). For developing experimental brain metastasis models by intracardiac (i.c.) inoculation, BALB/c-nu/nu mice were injected with MDA-MB-231 or OS-RC-2 cells (5×10^5 cells /mouse) by puncture into the left ventricle of the heart.

Clearing, 3D staining, and imaging of whole mouse brain samples were performed with CUBIC clearing and CUBIC-HistoVision (CUBIC-HV) staining protocols[6,9]. An updated CUBIC-HV staining protocol was used (HV1.1, commercialized by CUBICStars Co. and Tokyo Chemical Industry (TCI), TCI no. C3709, no. C3708). In brief, the PFA-fixed whole mouse brains were treated with CUBIC-L for 4 days at 37 °C, washed with PBS, stained with SYTOX-G (1/2500) in CUBIC-HV nuclear-staining buffer (included in TCI no. C3709) for 5 days at 37 °C, and then washed and immersed in 50% and 100% CUBIC-R+ for 1 day and 3 days, respectively, at room temperature. We used CUBIC-R+ (M) (45 wt% of antipyrine (TCI no. D1876), 30 wt% of *N*-methylnicotinamide (TCI no. M0374), and 0.5% (v/w) *N*-butyldiethanolamine (TCI no. B0725), adjusted to pH ~10) for brains containing cancer cells, and CUBIC-R+ (N) (45 wt% of antipyrine, 30 wt% of nicotinamide (TCI no. N0078), and 0.5% (v/w) *N*-butyldiethanolamine, adjusted to pH ~10) for the αSMA immunostained brain, respectively.

For the whole mouse brain immunostained with anti-α-SMA (Sigma, no. A5228) antibodies, the brain was subjected to CUBIC-HV immunostaining. The brain was first treated with 3 mg/mL hyaluronidase in CAPSO buffer (pH 10) for 24 hours at 37 °C. After washing with hyaluronidase wash buffer (50 mM carbonate buffer, 0.1% (v/v) Triton X-100, 5% (v/v) methanol, and 0.05% NaN_3) and HEPES-TSC buffer (10 mM HEPES buffer, pH 7.5, 10% (v/v) Triton X-100, 200 mM NaCl, 0.5% (w/v) casein, and 0.05% NaN_3), the brain was immersed in 500 µL of HEPES-TSC buffer containing a primary antibody (6 µg for anti-α-SMA), a secondary Fab fragment (FabuLight, Jackson immunolab, Alexa Fluor 594 goat anti-mouse IgG1 no. 115-587-185, Alexa Fluor 594 goat anti-rabbit IgG no. 111-587-008, Alexa Fluor 594 goat anti-mouse IgG2a no. 115-587-186, 1:0.75 of weight ratio), and 3D immunostaining additive (1×) (included in TCI no. C3708). Then, the sample was incubated with gentle shaking for 10 days at 32 °C. After staining, the sample was additionally incubated in the same buffer for 1 day at 4 °C to stabilize the Fab binding. Then, the sample was washed and post-fixed according to the protocol of CUBIC-HV immunostaining kit (TCI no. C3708) before being index-matched with CUBIC-R+. The cleared sample was embedded in CUBIC-R-agarose for imaging and storage[56]. For CUBIC-cleared tissues, which are less rigid than solvent-cleared tissues, agarose embedding helps to stabilize the tissues during imaging. This facilitates alignment of the resulting datasets across tiles and channels, as well as co-registration of ODO and NODO datasets. The animal experimental procedures and housing conditions of the animals were approved by the Animal Care and Use Committees of the Graduate School of Medicine of the University of Tokyo.

Quantification and image analysis of metastatic colonies. Quantitative morphological analysis of metastatic lumen and cancer cells (Fig. 3) were completed in Aivia 9.8.1 (Leica Microsystems, Bellevue, WA). First, Aivia's GPU accelerated machine learning-based Pixel Classifier was used to selectively enhance the contrast of cancer cells present within the lumen. The Pixel Classifier training data consisted of sparse cancer cells annotations within the metastatic blood vessel lumen over several *z*-planes and distributed throughout the ROI image volume (3 to 5 cells per *z*-plane were annotated). The annotations for the background regions included areas with no cells and cancer cells that were not colocalized with the lumen. Second, the output results from the pixel classifier were segmented and analyzed using the 3D Cell Analysis recipe. Here, the metastatic lumen was set as the top-level hierarchical object container and the cancer cells as individual objects contained within the lumen container. Morphological (for example, volume and surface area) and relational (for example overlapped volume percentage, contained cancer cell count) measurements were automatically calculated as part of the recipe workflow to characterize both cancer cell lines. Of the 34 total ROIs, 4 were excluded from the analysis (nos. 12, 19, 22, and 24 in Extended Data Fig. 1), as the imaging data did not capture the biological features being quantified in Fig. 3i–j.

Reporting Summary. Further information on research design is available in the Nature Research Reporting Summary linked to this article.

Data availability

The customized ZEMAX files, CAD files, list of components, and a summary of all datasets and the associated imaging parameters are available as **Supplementary Data**. Due to the large size of the imaging datasets collected within this manuscript, the datasets are not available in a public repository and are available from the authors upon request.

Code availability

The simulation codes used to model the lateral and axial resolution of the various microscope architectures is available on GitHub. The acquisition software code for the microscope is available from the authors upon request.

References

46. Keller, P. J. et al. Fast, high-contrast imaging of animal development with scanned light sheet-based structured-illumination microscopy. *Nat. Methods* **7**, 637–642 (2010).
47. Yueqian, Z. & Herbert, G. Systematic design of microscope objectives. Part I: system review and analysis. *Adv. Opt. Technol.* **8**, 313–347 (2019).
48. Hörl, D. et al. BigStitcher: reconstructing high-resolution image datasets of cleared and expanded samples. *Nat. Methods* **16**, 870–874 (2019).
49. Schindelin, J. et al. Fiji: an open-source platform for biological-image analysis. *Nat. Methods* **9**, 676–682 (2012).
50. Balazs, B., et al. A real-time compression library for microscopy images. Preprint at bioRxiv https://doi.org/10.1101/164624 (2017).
51. Chan, K. Y. et al. Engineered AAVs for efficient noninvasive gene delivery to the central and peripheral nervous systems. *Nat. Neurosci.* **20**, 1172–1179 (2017).
52. Chi, J. et al. Three-dimensional adipose tissue imaging reveals regional variation in beige fat biogenesis and PRDM16-dependent sympathetic neurite density. *Cell Metab.* **27**, 226–236.e3 (2018).
53. Ehata, S. et al. Transforming growth factor-β promotes survival of mammary carcinoma cells through induction of antiapoptotic transcription factor DEC1. *Cancer Res.* **67**, 9694 (2007).

54. Nishida, J. et al. Epigenetic remodelling shapes inflammatory renal cancer and neutrophil-dependent metastasis. *Nat. Cell Biol.* **22**, 465–475 (2020).
55. Miyoshi, H., Takahashi, M., Gage, F. H. & Verma, I. M. Stable and efficient gene transfer into the retina using an HIV-based lentiviral vector. *Proc. Natl Acad. Sci. USA* **94**, 10319–10323 (1997).
56. Matsumoto, K. et al. Advanced CUBIC tissue clearing for whole-organ cell profiling. *Nat. Protoc.* **14**, 3506–3537 (2019).

Acknowledgements

We would like to thank A. York and A. Millet-Sikking for discussions regarding oblique planar microscopy, remote focus imaging, and alignment procedures. We would also like to thank J. Daniels for discussions and his development of the multi-immersion objective, C. Shimizu (RIKEN BDR) for the support of preparing CUBIC-cleared and stained specimens, and K. Miyazono (The University of Tokyo) for the discussion and support of brain metastasis experiments. This work was funded in part by the National Institutes of Health (NIH) K99 CA240681 (A.K.G.), R01CA244170 (J.T.C.L.), R01EB031002 (J.T.C.L.), R01GM079712 (T.I.), R01DK107436 (L.X.), R01DK092202 (L.X.), R01MH117820 and R01NS104949 (R.C.R.); Department of Defense (DoD) Prostate Cancer Research Program (PCRP) W81XWH-18-10358 (J.T.C.L. and L.D.T.), W81XWH-19-1-0589 (N.P.R.), W81XWH-20-1-0039 (X.W.), and Prostate Cancer Young Investigator Award (N.P.R.); National Science Foundation (NSF) Graduate Research Fellowship DGE-1762114 (L.A.B. and K.W.B.); NSF 1934292 HDR: I-DIRSE-FW (J.T.C.L. and R.B.S.); Washington Research Foundation Postdoctoral Fellowship (C.R.S.); Science and Technology Platform Program for Advanced Biological Medicine by the Japan Agency for Medical Research and Development (AMED) JP21am0401011 (H.R.U.), ERATO by Japan Science and Technology Agency (JST) JPMJER2001 (H.R.U.), HFSP Research Grant Program RGP0019/2018 (H.R.U.), AMED-PRIME JP21gm6210027 (E.A.S.), Grants-in-Aid for Scientific Research on Innovative Areas (JSPS KAKENHI grant) 17H06328 (E.A.S.), Grants-in-Aid for Scientific Research on Innovative Areas (JSPS KAKENHI grant) 20K1612 (S.I.K.). Work in the Murawala laboratory is supported by grants from NIH-COBRE (5P20GM104318-08) and DFG (429469366). Work in the Dodt laboratory is supported by grants FWF P31263-B26 and WWTF CS19-019.

Author contributions

A.K.G. and J.T.C.L. conceived of and designed the microscope system. P.R.N. provided feedback on the system design and its potential applications. A.K. G., K.W.B., R.B.S., and G.G. performed simulations of the microscope. A.K.G. fabricated the microscope system with help from L.A.B.E.A.S. and H.R.U. provided and prepared the immunostained CUBIC-cleared mouse brains. E.A.S., S.I.K., and H.R.U. prepared and provided the metastatic mouse brains. J.C. and K.S. prepared and provided the mouse brain. P.B., E.T., and R.C.R. provided the mouse brain with preparation by A.K.G. The human brain slice was prepared by A.K.G.H.L. and L.A.G.L. provided quantitative analysis of the high-resolution images. Y.Y. and H.Z. provided and prepared the PEGASOS-cleared mouse brain. E.K.N., B.J.B., and J.S. provided and prepared the SHIELD-cleared mouse embryos. H.H., N.P.R., and L.D.T. provided and prepared the ECi-cleared human prostate tissue. J.J.W., R.S., E.S., C.R.S., and M.Y.G. provided and prepared the Ce3D-cleared mouse lymph node. X.W. and L.X. provided and prepared the iDISCO-cleared mouse prostate. A.K.H. and T.I. provided and prepared the ClearSee-processed Arabidopsis plant and M.P., P.M., and H.U.D. provided and prepared the DEEP-Clear-processed Axolotl. A.K.G. and J.T.C.L. led the writing of the manuscript. All authors contributed to the manuscript.

Competing interests

A.K.G., N.P.R., L.D.T., and J.T.C.L. are co-founders and shareholders of Alpenglow Biosciences. L.A.G.L. and H.L. are employees of Leica Microsystems, maker of the Aivia software.

Additional information

Extended data is available for this paper at https://doi.org/10.1038/s41592-022-01468-5.

Supplementary information The online version contains supplementary material available at https://doi.org/10.1038/s41592-022-01468-5.

Correspondence and requests for materials should be addressed to Adam K. Glaser or Jonathan T. C. Liu.

Peer review information *Nature Methods* thanks Peter Santi, Per Uhlen, and Fabian Voigt for their contribution to the peer review of this work. Rita Strack was the primary editor on this article and managed its editorial process and peer review in collaboration with the rest of the editorial team.

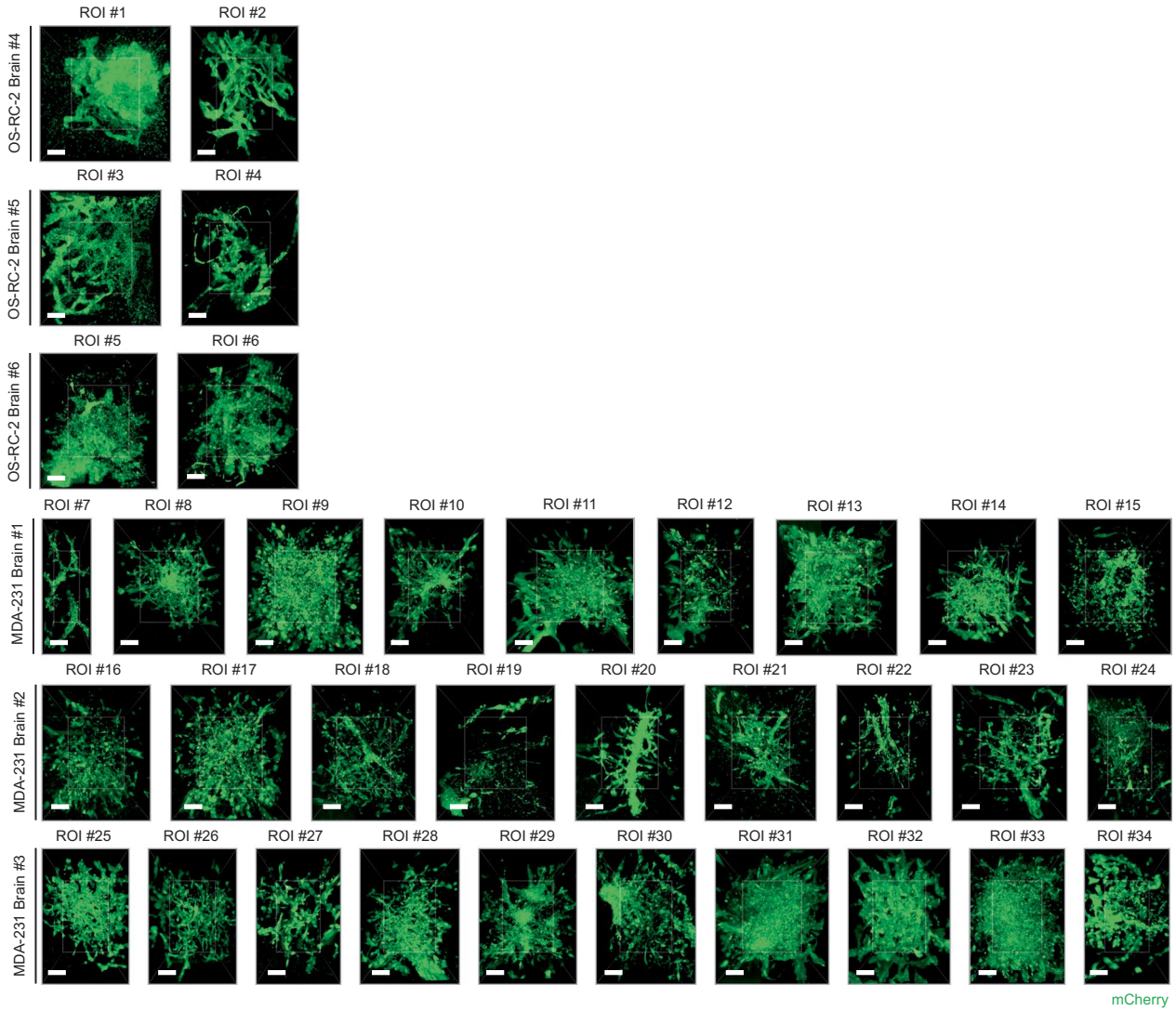

Extended Data Fig. 1 | Regions of interests from metastatic brain specimens. All $n = 34$ metastatic colonies collected from the metastatic brain specimens (3 brains from OS-RC-2 cancer cell line, 3 brains from MDA-MB-231 cancer cell line). All scale bars represent 10 μm.

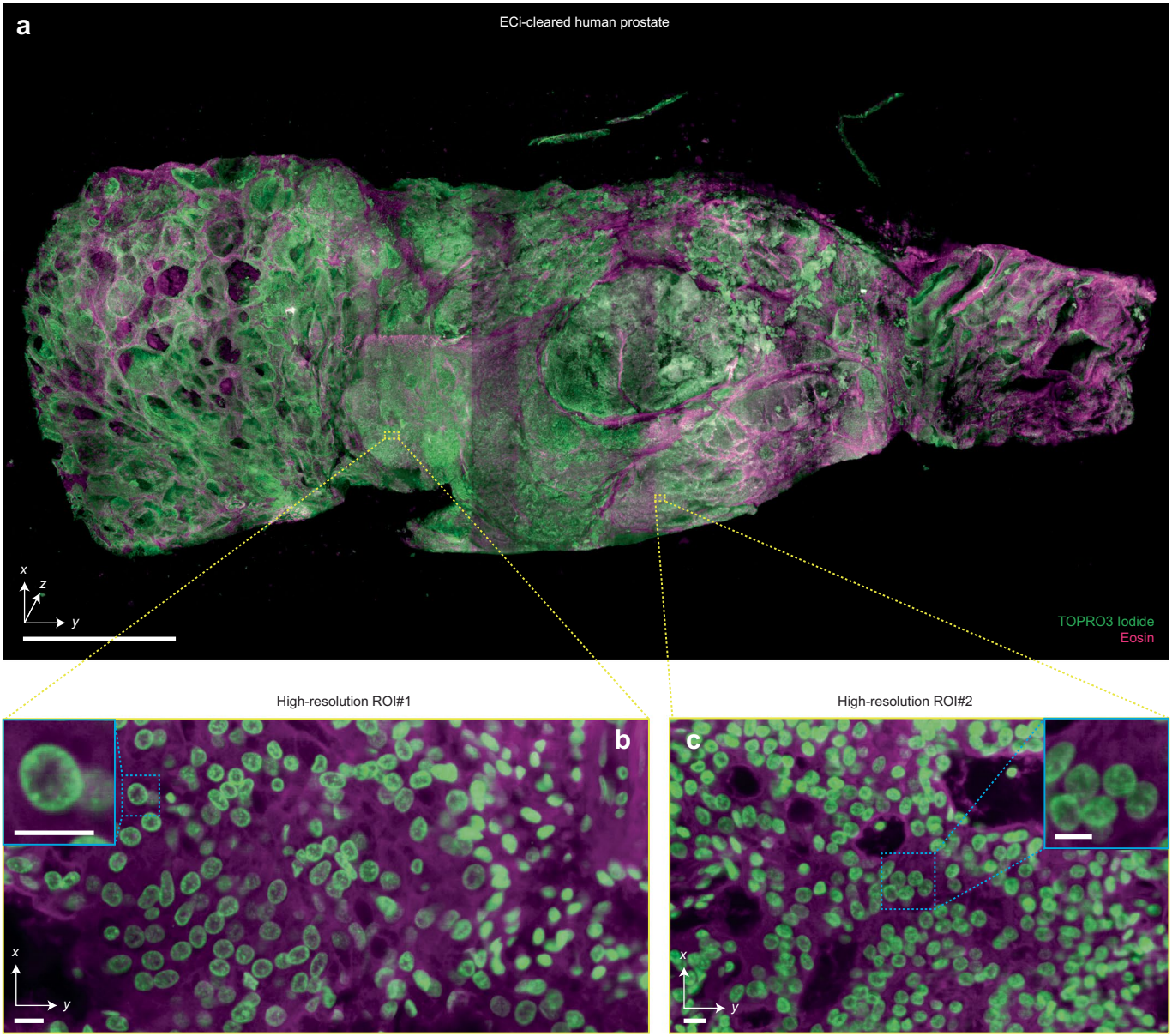

Extended Data Fig. 2 | Multi-scale 3D pathology of human prostate tissue. (a) Fast meso-scale screening results for a multi-cm-sized piece of human prostate tissue stained with TO-PRO-3 Iodide (nuclear) and Eosin. Representative high-resolution regions of interests for two different foci of cancer are shown in **(b)** and **(c)**. The insets demonstrate the ability to clearly resolve sub-nuclear features in cancer nuclei. Scale bar lengths are as follows: **(a)** 1 cm, **(b)** and **(c)** 10 μm. The imaging data in **(a-c)** was acquired from in a single experiment, which was not repeated.

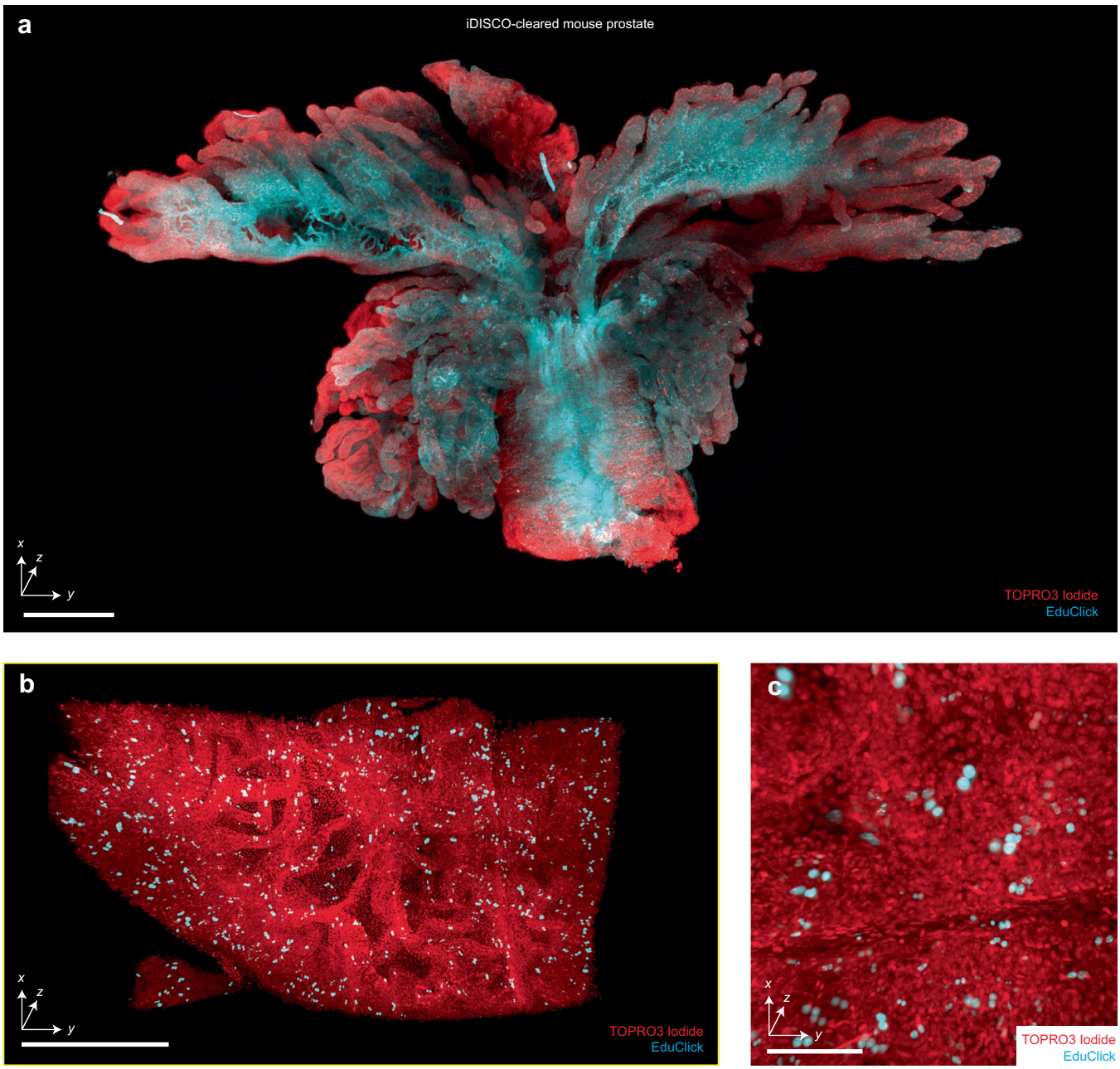

Extended Data Fig. 3 | Assessment of 3D cell proliferation assays with iDISCO. (a) Screening of an intact mouse prostate cleared using iDISCO, labeled with TOPRO3 Iodide (nuclear) and an EduClick cell-proliferation marker. A higher-resolution region of interest focused on a prostate gland is shown in **(b)**. An additional zoomed-in view showing the ability to resolve individual proliferating nuclei **(c)**. Scale bars lengths are as follows: **(a)** 1mm, **(b)** 200 µm, and **(c)** 100 µm. The imaging data in **(a-c)** was acquired from in a single experiment, which was not repeated.

Extended Data Fig. 4 | Imaging of non-rodent and non-human tissues. (a) Hybrid open-top light-sheet imaging of a ClearSee-cleared Arabidopsis specimen. **(b)** Higher-resolution imaging of the Arabidopsis root. **(c)** Meso-scale imaging of a large multi-cm Axolotl cleared with DEEP-Clear. Scale bars lengths are as follows: **(a)** 1 mm, **(b)** 100 µm, and **(c)** 1 cm. The imaging data in **(a-c)** was acquired from in a single experiment, which was not repeated.

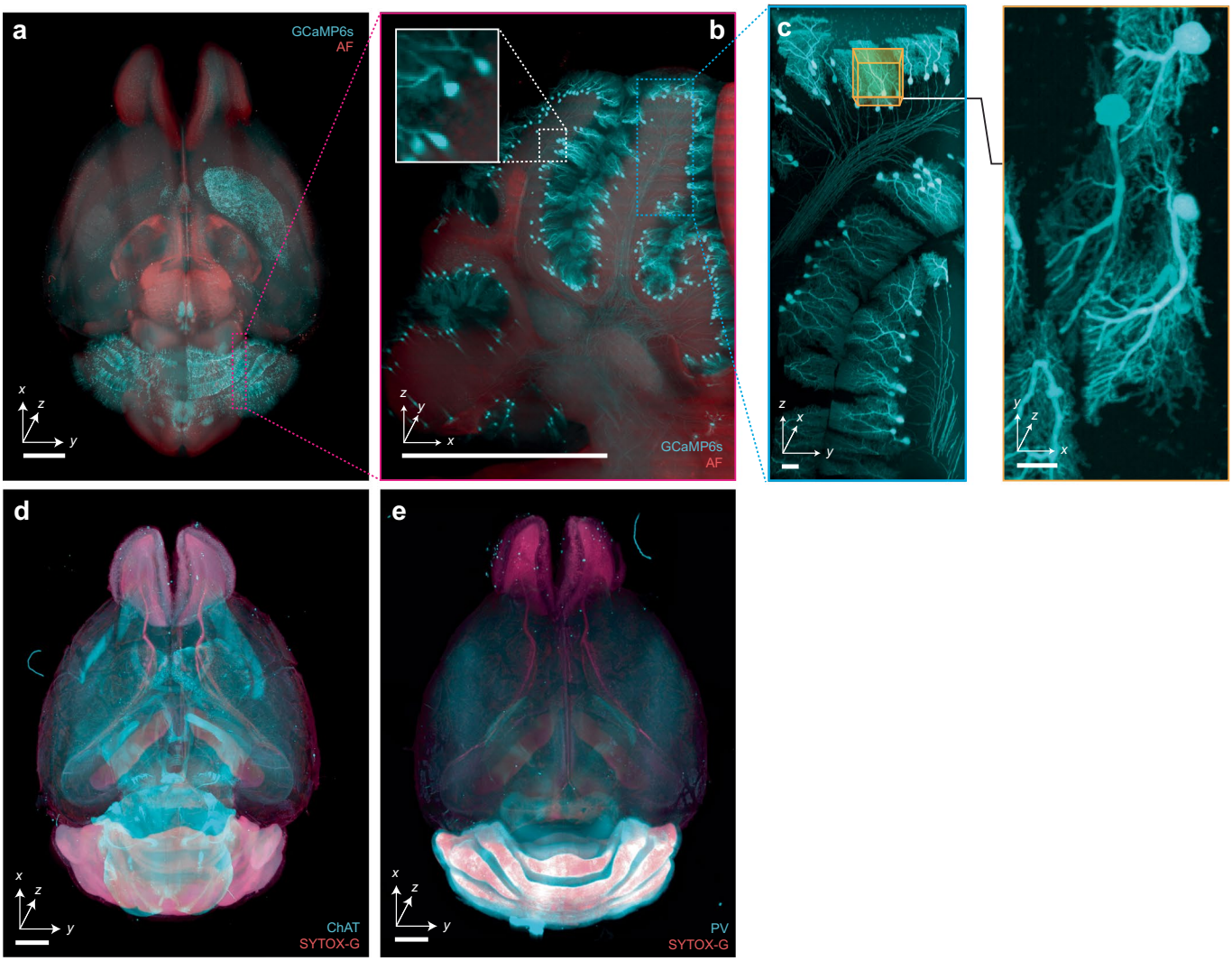

Extended Data Fig. 5 | Imaging of immunostained and endogenously fluorescent CUBIC-cleared mouse brains. Hybrid OTLS imaging of whole mouse brains. **(a-c)** with endogenously preserved GCaMP6s fluorescence, and immunostained with **(d)** anti-ChAT antibody + SYTOX-G or **(e)** anti-Parvalbumin (PV) antibody + SYTOX-G by CUBIC-HistoVision. Scale bar lengths are as follows: **(a-b)** 1 mm, **(c)** 10 μm, **(d-e)** 2 mm. The imaging data in **(a-e)** was acquired from in a single experiment, which was not repeated.

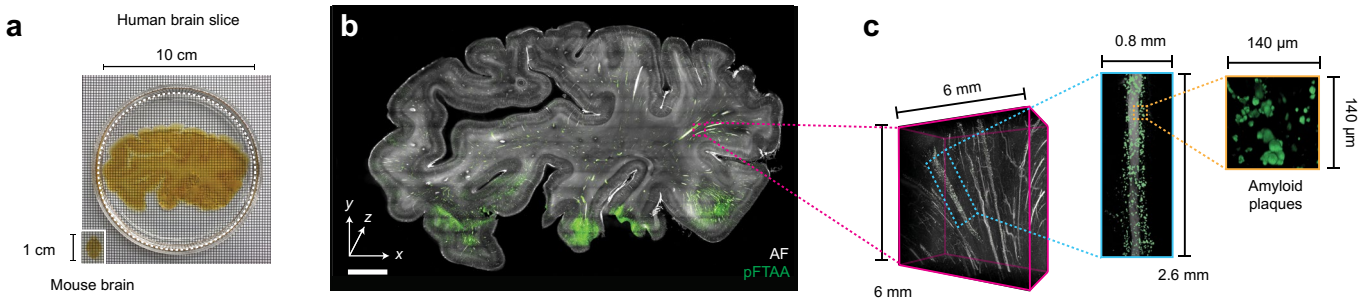

Extended Data Fig. 6 | Large-scale imaging of thick human tissues. (a) Slab of human brain tissue after CUBIC clearing. A mouse brain is shown for size comparison. (b) ODO imaging results of the entire 3-mm thick brain slab. Autofluorescence is shown in black and white, and the amyloid small molecule stain (pFTAA) is shown in green. (c) Zoom-in views of an amyloid-rich region reveal perivascular accumulation. Scale bar lengths are as follows: (b) 1 cm. The imaging data in (a-c) was acquired from in a single experiment, which was not repeated.

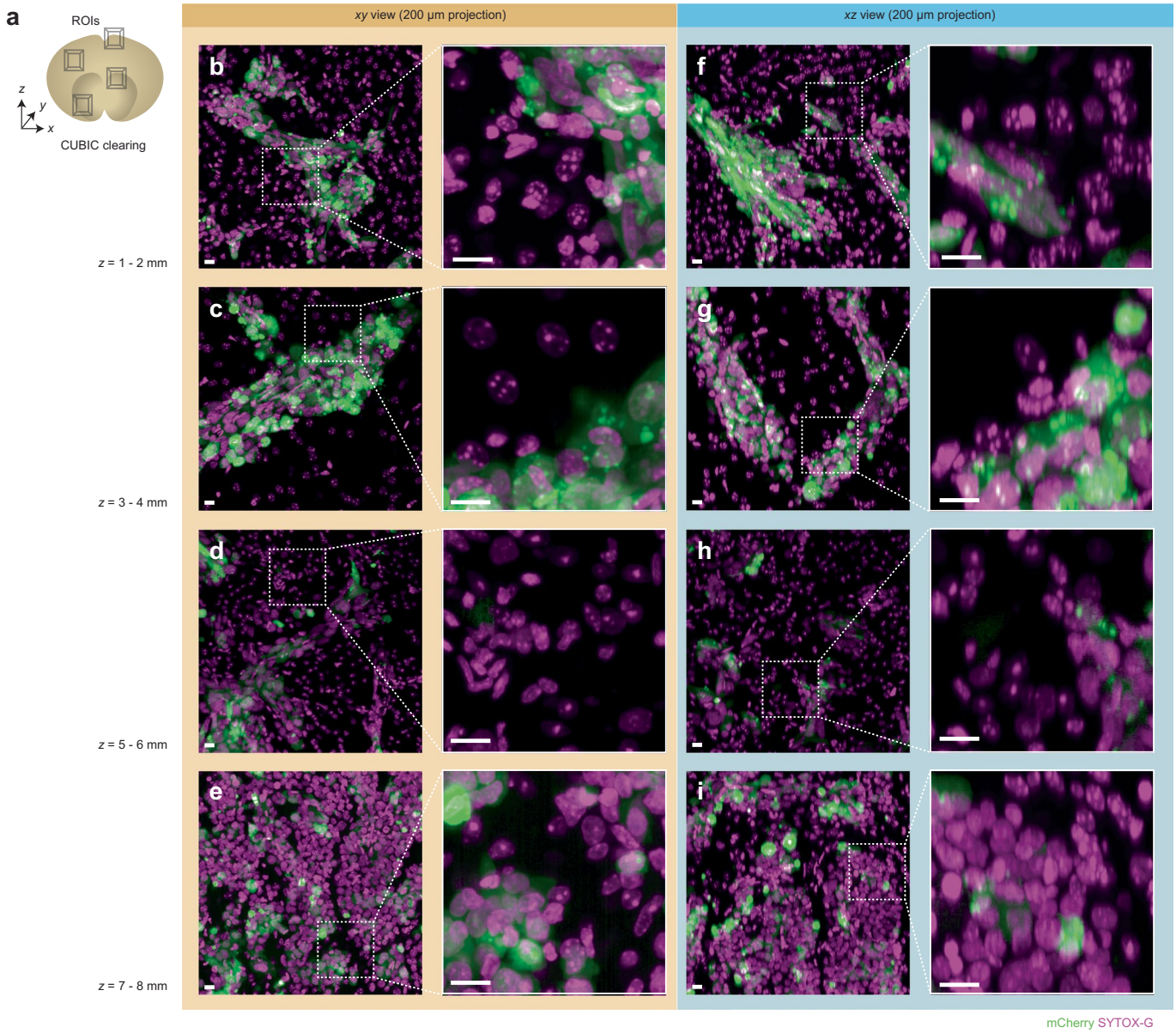

Extended Data Fig. 7 | NODO imaging quality versus imaging depth in a CUBIC-cleared mouse brain. (a) Multiple two-channel regions of interest (ROIs) were acquired from a CUBIC-cleared mouse brain at various imaging depths ($z = 1$–8 mm). (b-e) *xy* views for ROIs at various depths are shown. The corresponding xz views of each ROI are shown in (f-i). The high-magnification insets show fine sub-nuclear details and demonstrate that there is minimal degradation in image quality as a function of depth. All scalebars denote 10 µm. The imaging data in (b-i) was acquired from in a single experiment, which was not repeated.

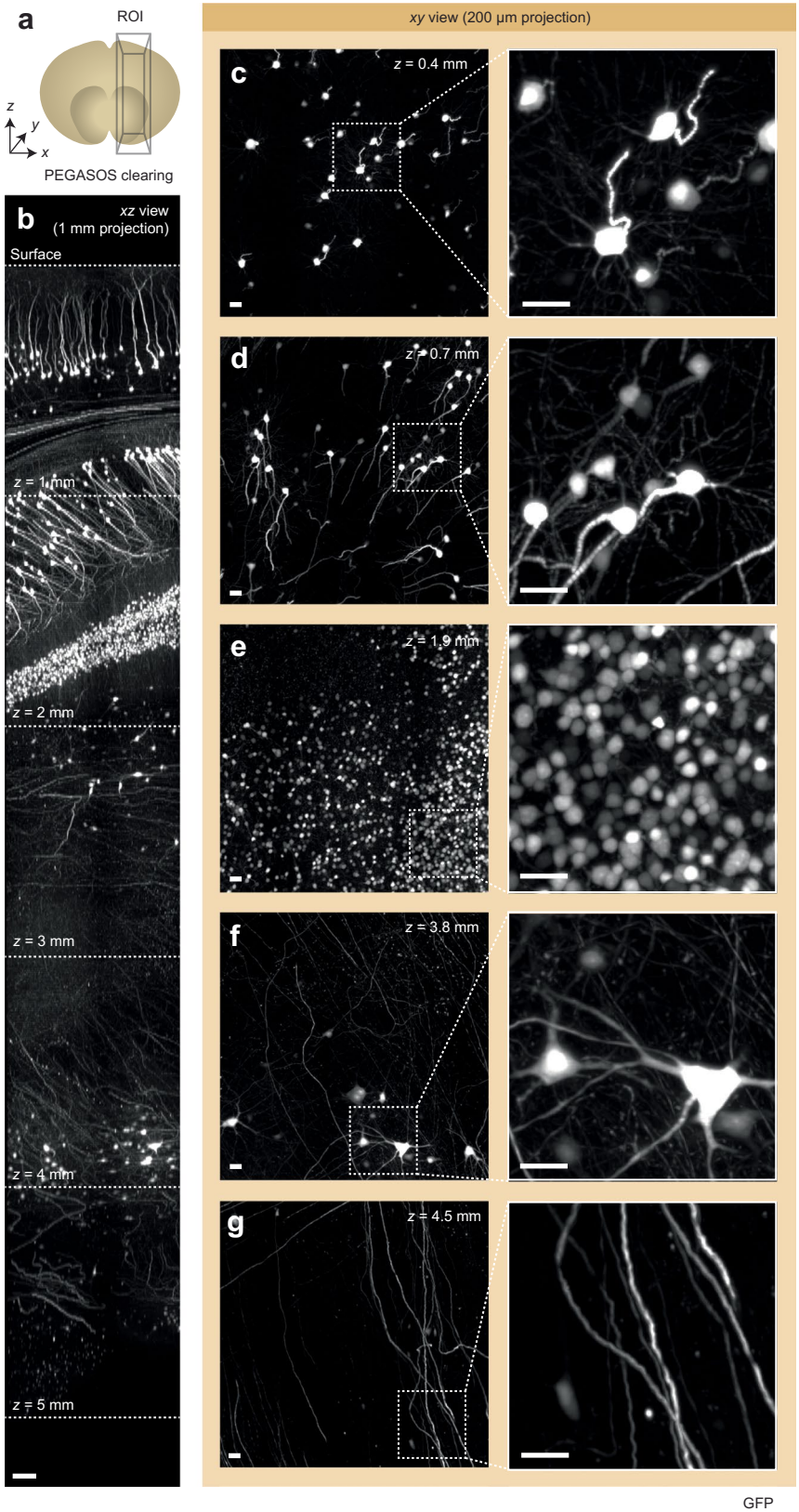

Extended Data Fig. 8 | NODO imaging quality versus imaging depth in a PEGASOS-cleared mouse brain. (a) A single ROI was acquired from a PEGASOS-cleared mouse brain. (b) xz view of the ~5 mm deep ROI, demonstrating near-consistent image quality versus depth. (c-g) *xy* views for ROIs at various depths are shown. The high-magnification insets show fine sub-nuclear details and demonstrate that there is minimal degradation in image quality as a function of depth. Scale bar lengths are as follows: (b) 100 µm, (c-g) 10 µm. The imaging data in (b-g) was acquired from in a single experiment, which was not repeated.

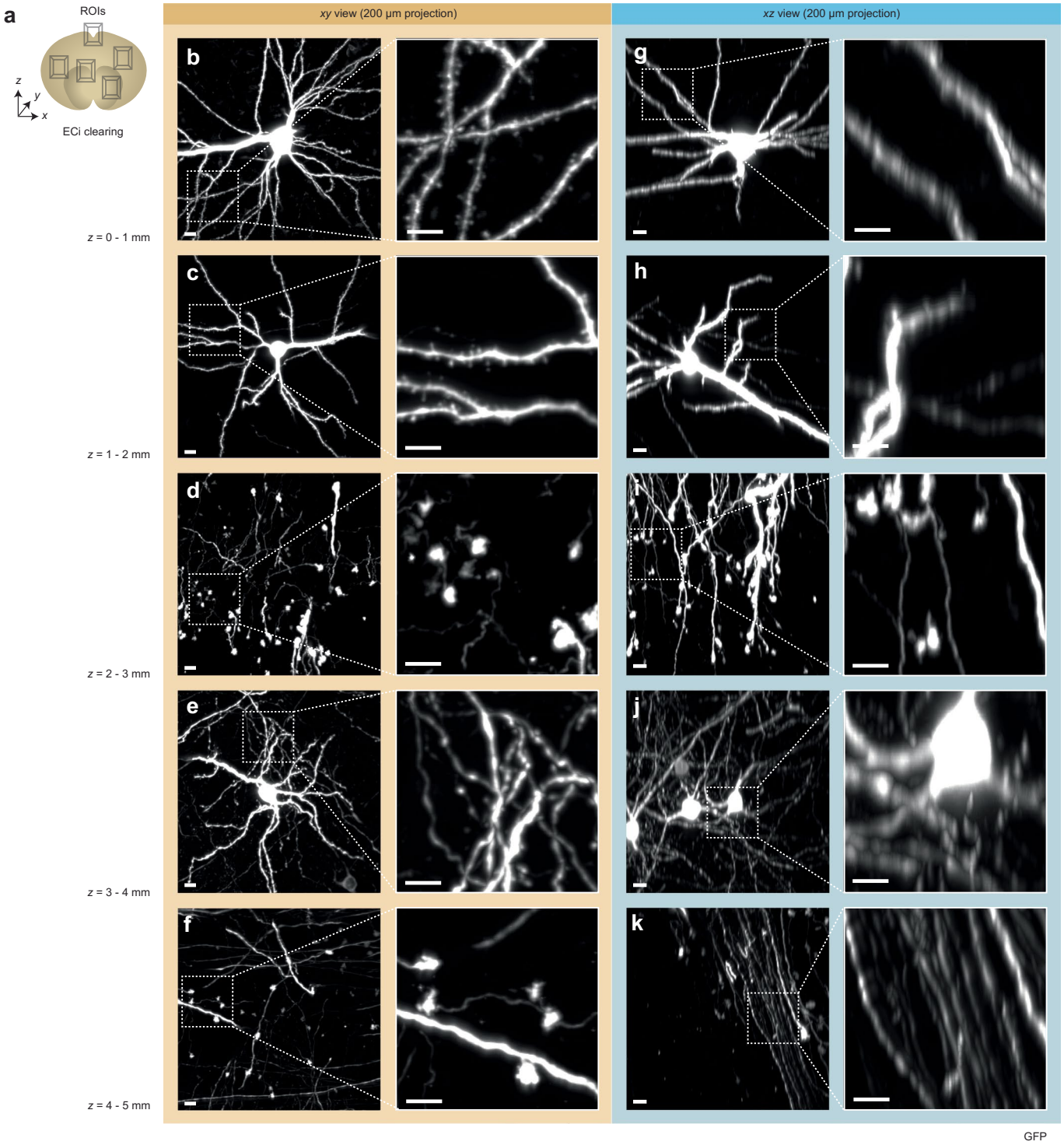

Extended Data Fig. 9 | NODO imaging quality versus imaging depth in an ECi-cleared mouse brain. (a) Multiple regions of interest (ROIs) were acquired from an ECi-cleared mouse brain at various imaging depths ($z = 0–5$ mm). (b-f) *xy* views for ROIs at various depths are shown. The corresponding xz views of each ROI are shown in (g-k). The high-magnification insets show fine sub-nuclear details and demonstrate that there is minimal degradation in image quality as a function of depth. All scalebars denote 10 µm. The imaging data in (b-k) was acquired from in a single experiment, which was not repeated.

nature portfolio

Corresponding author(s): Adam Glaser

Last updated by author(s): Mar 9, 2022

Reporting Summary

Nature Portfolio wishes to improve the reproducibility of the work that we publish. This form provides structure for consistency and transparency in reporting. For further information on Nature Portfolio policies, see our Editorial Policies and the Editorial Policy Checklist.

Statistics

For all statistical analyses, confirm that the following items are present in the figure legend, table legend, main text, or Methods section.

n/a	Confirmed
☐	☒ The exact sample size (*n*) for each experimental group/condition, given as a discrete number and unit of measurement
☐	☒ A statement on whether measurements were taken from distinct samples or whether the same sample was measured repeatedly
☐	☒ The statistical test(s) used AND whether they are one- or two-sided *Only common tests should be described solely by name; describe more complex techniques in the Methods section.*
☒	☐ A description of all covariates tested
☒	☐ A description of any assumptions or corrections, such as tests of normality and adjustment for multiple comparisons
☐	☒ A full description of the statistical parameters including central tendency (e.g. means) or other basic estimates (e.g. regression coefficient) AND variation (e.g. standard deviation) or associated estimates of uncertainty (e.g. confidence intervals)
☐	☒ For null hypothesis testing, the test statistic (e.g. *F*, *t*, *r*) with confidence intervals, effect sizes, degrees of freedom and *P* value noted *Give P values as exact values whenever suitable.*
☒	☐ For Bayesian analysis, information on the choice of priors and Markov chain Monte Carlo settings
☒	☐ For hierarchical and complex designs, identification of the appropriate level for tests and full reporting of outcomes
☒	☐ Estimates of effect sizes (e.g. Cohen's *d*, Pearson's *r*), indicating how they were calculated

Our web collection on statistics for biologists contains articles on many of the points above.

Software and code

Policy information about availability of computer code

Data collection	A custom-written Python software was used to operate the microscope system and collect data for this study. This software is available from the authors upon request.
Data analysis	Data is processed using a combination of commercial, open-source, and custom written code. Open-source tools used include HDF5 (1.8.18) (https://www.hdfgroup.org/solutions/hdf5/), a B3D compression filter for HDF5 files (https://git.embl.de/balazs/B3D) commit SHA (e77582ffa804b8dbe5d0e6db0f1f660b47e19ef0), Python (3.6.1) and required packages, and BigStitcher (0.7.0) for visualizing and stitching the tiled imaging data (https://imagej.net/BigStitcher). Fiji (ImageJ 1.53c) was used to quantify the line profiles of axons in Figure 2. Aivia 9.8.1 was used to segment the regions of interest presented in Figure 3. The PSF simulations were conducted using publicly available code at: https://github.com/adamkglaser/OPM_simulations.

For manuscripts utilizing custom algorithms or software that are central to the research but not yet described in published literature, software must be made available to editors and reviewers. We strongly encourage code deposition in a community repository (e.g. GitHub). See the Nature Portfolio guidelines for submitting code & software for further information.

Data

Policy information about availability of data

All manuscripts must include a data availability statement. This statement should provide the following information, where applicable:

- Accession codes, unique identifiers, or web links for publicly available datasets
- A description of any restrictions on data availability
- For clinical datasets or third party data, please ensure that the statement adheres to our policy

The customized ZEMAX files, CAD files, list of components, and a summary of all datasets and the associated imaging parameters are available as Supplementary

Data. Due to the large size of the imaging datasets collected within this manuscript, the datasets are not available in a public repository and are available from the authors upon request.

Field-specific reporting

Please select the one below that is the best fit for your research. If you are not sure, read the appropriate sections before making your selection.

☒ Life sciences ☐ Behavioural & social sciences ☐ Ecological, evolutionary & environmental sciences

For a reference copy of the document with all sections, see nature.com/documents/nr-reporting-summary-flat.pdf

Life sciences study design

All studies must disclose on these points even when the disclosure is negative.

Sample size	We did not calculate sample sizes beforehand. For the metastatic brains, the total number of brains (n = 6) and total number of regions of interest (n = 34) was informed by a previous study (Kubota, S.I., et al., Whole-Body Profiling of Cancer Metastasis with Single-Cell Resolution. Cell Reports, 2017. 20(1): p. 236-250). These sample sizes were justified posteriori as the subsequent analysis was found to be statistically significant. For microscope point spread function measurements, tbhe performance is generally highly repeatable/reproducible, as the results are deterministic and based upon optical principles and any systematic aberrations in a system. As a result, it is common for imaging/microscopy papers to measure point spread functions by averaging a handful of beads. For this study, we estimated point spread functions over the imaging field of view of both the ODO and NODO path, and averaged the results of many beads (n = 109 beads for the NODO path, n = 437 for the ODO path). These numbers were dictated by the density and total imaging volume used to quantify the point spread function.
Data exclusions	Of the 34 regions of interest imaged from the metastatic brain samples, 4 were excluded, as these regions of interest were spurious, where the majority of the imaging data was void of signal / the biological features being analyzed in Fig. 3i-j were absent.
Replication	We checked imaging performance for an array of specimen types and clearing protocols, as demonstrated through the various imaging datasets presented within the main figures extended data figures, and supplementary figures of this manuscript. Replications of the imaging performance was successful in each case.
Randomization	For all ODO imaging results in this manuscript, the entire specimen was imaged. Therefore randomization was not applicable. For targeted NODO imaging, the sub-regions were chosen based on morphological features (Fig. 1 and 2) or the presence of a metastatic colony (Fig. 3). Therefore randomization was not applicable.
Blinding	The purpose of this manuscript was to present a new imaging method, and therefore blinding is not applicable.

Reporting for specific materials, systems and methods

We require information from authors about some types of materials, experimental systems and methods used in many studies. Here, indicate whether each material, system or method listed is relevant to your study. If you are not sure if a list item applies to your research, read the appropriate section before selecting a response.

Materials & experimental systems

n/a	Involved in the study
☐	☒ Antibodies
☐	☒ Eukaryotic cell lines
☒	☐ Palaeontology and archaeology
☐	☒ Animals and other organisms
☒	☐ Human research participants
☒	☐ Clinical data
☒	☐ Dual use research of concern

Methods

n/a	Involved in the study
☒	☐ ChIP-seq
☒	☐ Flow cytometry
☒	☐ MRI-based neuroimaging

Antibodies

Antibodies used	Anti-GFP (Abcam, #ab290) 1:1000 dilution Anti-α-SMA (Sigma, #A5228) 6 µg in 500 µL of HEPES-TSC buffer (based on total mAb weight per brain - not dilution) Anti-PV (Swant, #PV235) 1:50 dilution, 10 µL in 500 µL of HEPES-TSC buffer Anti-ChAT (Abcam, #ab178850) 5.3 µg in 500 µL of HEPES-TSC buffer (based on total mAb weight per brain - not dilution) AlexaFluor®594 Goat Anti-Mouse IgG1 (FabuLight, Jackson immunolab, #115-587-185) AlexaFluor®594 Goat Anti-Rabbit IgG (FabuLight, Jackson immunolab, #111-587-008) AlexaFluor®594 Goat Anti-Mouse IgG2a (FabuLight, Jackson immunolab, #115-587-186) SIRPa-CF594 (BioLegend #144002) 1:200 dilution, 2.5 µL in 500 µL

CD11c-BV480 (Fisher Scientific #746392) 1:200 dilution, 2.5 µL in 500 µL
CD31-AlexaFluor®488 (BioLegend #102514) 1:200 dilution, 2.5 µL in 500 µL
CD3-BV421 (BioLegend #100228) 1:200 dilution, 2.5 µL in 500 µL

Validation

Anti-GFP (Abcam, #ab290) was previously validated in: Reconstruction of 1,000 Projection Neurons Reveals New Cell Types and Organization of Long-Range Connectivity in the Mouse Brain, Winnubst, Johan et al. Cell, Volume 179, Issue 1, 268 - 281.e13

Anti-α-SMA (Sigma, #A5228), Anti-PV (Swant, #PV235), Anti-ChAT (Abcam, #ab178850), AlexaFluor®594 Goat Anti-Mouse IgG1 (FabuLight, Jackson immunolab, #115-587-185), AlexaFluor®594 Goat Anti-Rabbit IgG (FabuLight, Jackson immunolab, #111-587-008), AlexaFluor®594 Goat Anti-Mouse IgG2a (FabuLight, Jackson immunolab, #115-587-186) were previously validated in: Susaki, E.A., Shimizu, C., Kuno, A. et al. Versatile whole-organ/body staining and imaging based on electrolyte-gel properties of biological tissues. Nat Commun 11, 1982 (2020). https://doi.org/10.1038/s41467-020-15906-5

SIRPa-CF594 (BioLegend #144002) and CD11c-BV480 (Fisher Scientific #746392) were previously validated in: Stoltzfus, C.R., et al., CytoMAP: A Spatial Analysis Toolbox Reveals Features of Myeloid Cell Organization in Lymphoid Tissues. Cell Rep, 2020. 31(3): p. 107523.

Eukaryotic cell lines

Policy information about cell lines

Cell line source(s)

Human breast cancer cells, MDA-MB-231-5a-D, was derived from the parental MDA-MB-231 line as described previously (Ehata et al., 2007). Human renal cancer cells, OS-RC-2 was derived from RIKEN Cell Bank (Tsukuba, Japan).

Authentication

MDA-MB-231-5a-D cell line were validated as having the same STR profile as parental MDA-MB-231 cell line (BEX Co Ltd., Tokyo, Japan). OS-RC-2 were validated using STR Profiling at the BEX Co Ltd. (Tokyo, Japan).

Mycoplasma contamination

Routine mycoplasma contamination testing was performed by PCR regularly on these cells. Testing results were negative for contamination.,

Commonly misidentified lines
(See ICLAC register)

No commonly misidentified cell lines were used in this study.

Animals and other organisms

Policy information about studies involving animals; ARRIVE guidelines recommended for reporting animal research

Laboratory animals

The following mice were used:
- BALB/c-nu/nu
- C57BL/6
- C57BL/6N
- Slc17a7-Cre
- Ly5.1
- Chat-IRES-Cre;Ai162
- Slc17a7-IRES2-Cre;Ai14
- Thy1-eGFP-M
- C57BL/6J (WT) and B6.129(Cg)-Gt(ROSA)26Sortm4(ACTB-tdTomato,-EGFP)Luo/J ("mTmG"). Female WT mice at least 7 weeks old were bred to male mTmG+/+ mice; first day of plug positive was marked as embryonic day (E)0.5. On E12.5 or E13.5, dams were euthanized and mTmG+/- embryos were collected.

Wild animals

No wild animals were used in this study.

Field-collected samples

No field collected samples were used in this study.

Ethics oversight

All experiments (Figure 1,3, Extended Data Figure 5d,e, Extended Data Figure 7) were approved and carried out according to the Animal Care and the Use Committee of the Graduate School of Medicine, The University of Tokyo.

All experimental protocols (Figure 2, Extended Data Figure 9) were conducted according to the National Institutes of Health guidelines for animal research and were approved by the Institutional Animal Care and Use Committee at Howard Hughes Medical Institute, Janelia Research Campus.

De-identified fresh prostate tissues (Extended Data Figure 2) were obtained prospectively from a genitourinary biorepository (approved by the University of Washington Institutional Review Board, IRB), with patient consent.

All procedures (Extended Data Figure 3, Supplementary Figure 19,20) were approved by the University of Washington Institutional Animal Care and Use Committee.

The Axolotl used in this experiment (Extended Data Figure 4) are approved by MDIBL IACUC committee (no.# 20-04).

All procedures involving transgenic mice (Extended Data Figure 5a-c) were conducted in accordance with NIH guidelines and approved by the Institutional Animal Care and Use Committee (IACUC) of the Allen Institute for Brain Science.

Human brain tissue from an Alzheimer's disease donor was obtained from the University of Washington Biorepository and Integrated Neuropathology (BRaIN) Laboratory (Extended Data Figure 6).

Procedures involving mice were approved by the Institutional Animal Care and Use Committee of Texas A&M in accordance with NIH guidelines (Extended Data Figure 8, Supplementary Figure 18).

Note that full information on the approval of the study protocol must also be provided in the manuscript.